INTERREG-V OCEAN INDIEN 2014-2020

Projet de Recherche

RENOVRISK-CYCLONES ET CHANGEMENT CLIMATIQUE

Axe-1 OT-1 OS-01a - Action I-3 TF

Livrable 8

Jeux de données - Séries temporelles et climatologie des mesures physiques de houle, mises en ligne sur un serveur de l'Université et rapport décrivant les données acquises.

Emmanuel Cordier, OSU-R

Mars 2021

Ce livrable est associé à la sous-action intitulée :

Observation terrestre et marine de la houle

Il consiste en:

1 / Un jeu de données mis en ligne sur le serveur de l'université de La Réunion accessible au lien suivant :

ftp://renovrisk-gnss@tramontane.univ-reunion.fr:21

mdp: f1X2tA356Byb64T6

Répertoire: Swell-data

2/ Un article scientifique décrivant les instruments, résultats obtenus et données acquises (Section 3.1 - p 9-17)

atmosphere

MDPI

Article

Impact of Tropical Cyclones on Inhabited Areas of the SWIO Basin at Present and Future Horizons: Overview and Observing Component of the Research Project RENOVRISK-CYCLONE

Olivier Bousquet[1,2*], Guilhem Barruol[3], Emmanuel Cordier[4], Christelle Barthe[1,5], Soline Bielli[1], Radiance Calmer[1,6], Elisa Rindraharisaona[7], Gregory Roberts[6,8], Pierre Tulet[1,5], Vincent Amelie[9], Frauke Fleischer-Dogley[10], Alberto Mavume[11], Jonas Zucule[12], Lova Zakariasy[13], Bruno Razafindradina[13], François Bonnardot[14], Manvendra Singh[15], Edouard Lees[1], Jonathan Durand[1], Dominique Mekies[1], Marine Claeys[1,8], Joris Pianezze[1], Callum Thompson[1], Chia-Lun Tsai[1,16], Romain Husson[17], Alexis Mouche[18], Stephane Ciccione[19], Julien Cattiaux[8], Fabrice Chauvin[8], Nicolas Marquestaut[1,4]

[1] Laboratoire de l'Atmosphère et des Cyclones (UMR8105 LACy), Université de La Réunion, CNRS, Météo-France), Saint Denis de La Réunion, France
[2] Institute for Coastal Marine Research CMR), Nelson Mandela University, Port-Elizabeth, RSA
[3] Université de Paris, Institut de Physique du Globe de Paris, CNRS, Paris, France
[4] Observatoire de Sciences de l'Univers de La Réunion (UMS 3365 OSU-R), Saint Denis de La Réunion, France
[5] Laboratoire d'Aérologie, Université de Toulouse, UT3, CNRS, IRD, Toulouse, France
[6] Scripps Institution of Oceanography, University of California, San Diego, CA, USA
[7] Laboratoire GéoSciences Réunion (LGSR), Université de La Réunion, Saint Denis de La Réunion, France
[8] Centre National de recherche Météorologique (UMR3589 CNRM), Météo-France, Université de Toulouse, CNRS, Toulouse, France
[9] Seychelles Meteorological Authority, Mahé, Seychelles
[10] Seychelles Islands Foundation, Mahé, Seychelles
[11] Eduardo Mondlane University, Maputo, Mozambique
[12] Instituto Nacional de Meteorologia (INAM), Maputo, Mozambique
[13] Institut Supérieur de Technologie d'Antsiranana, Antsiranana, Madagascar
[14] Direction Interrégionale de Météo-France pour l'Océan Indien, Saint-Denis, Réunion
[15] Mauritius Oceanography Institute, Albion, Mauritius
[16] Department of Astronomy and Atmospheric Sciences, Center for Atmospheric REmote Sensing (CARE), Kyungpook National University, Daegu, South Korea
[17] Collecte Localisation Satellites (CLS), Brest, France
[18] Laboratoire d'Océanographie Physique et Spatiale, Ifremer, Plouzané, France
[19] Kelonia, Observatoire des tortues marines de La Réunion, Saint-Leu, France

* Correspondence: olivier.bousquet@meteo.fr

Citation: Lastname, F.; Lastname, F.; Lastname, F. Title. *Atmosphere* **2021**, *12*, x. https://doi.org/10.3390/xxxxx

Academic Editor: Firstname Lastname

Received: date
Accepted: date
Published: date

Abstract: The international research program "ReNovRisk-CYCLONE" (RNR-CYC, 2017-2021) directly involves 20 partners from 5 countries of the South-West Indian-Ocean. It aims at improving the observation and modelling of tropical cyclones in the South-West Indian Ocean, as well as to foster regional cooperation and improve public policies adapted to present and future tropical cyclones risk in this cyclonic basin.

This paper describes the structure and main objectives of this ambitious research project with emphasis on its observing components, which allowed integrating numbers of innovative atmospheric and oceanic observations (sea-turtle borne and seismic data, unmanned airborne system, ocean gliders), as well as combining standard and original methods (RS and GNSS atmospheric soundings, seismic and ADCP sampling, drone and satellite imaging) to support research on tropical cyclones from the local to the basin-scale.

Keywords: Tropical Cyclone; South-West Indian Ocean; Gliders; Unmanned Airborne System; Biologging; Global Satellite Navigation System; ReNovRisk; Numerical Modelling; Climate modelling; Austral and cyclonic swells; Seismic data

1. Introduction

Due to their highly destructive potential, tropical cyclones (TC) have long been considered as a major risk for populations, territorial economies and biodiversity. In this regard, predicting their outcome and impacts at present and future times is one of the major concerns of both the Intergovernmental Panel on Climate Change (IPCC) and the World Meteorological Organization (WMO).

As highlighted in the latest reports of WMO's International Workshop on Tropical Cyclones (IWTC), research work carried out over the last four years has considerably improved our understanding of TC intensification process [1,2] as well as TC track and intensity forecasting [3,4]. The operational implementation of coupled ocean-atmosphere (OA) numerical weather prediction (NWP) systems by many national weather services has, in particular, played a key role in reducing forecasting errors at all space and time scales (e.g., [5-8]). Despite these important advances, additional efforts are still needed to accurately predict and characterize the potential impacts of tropical cyclones on a given territory, especially during landfall. Such efforts include for instance the collection of novel atmospheric and oceanic observations, to better constrain (and verify) the performance of coupled NWP systems (e.g., [9,10]), as well as the implementation of wave models and specific microphysical parameterizations to improve roughness, swell, wind speed and momentum flux representation in TC forecasting systems [11-13].

Accurate modelling of OA interactions is particularly crucial in areas such as the tropical South-West Indian Ocean (SWIO) basin [30-90°E, 0-40°S], where the atmospheric variability is associated with a particularly strong oceanic response (and vice versa). The SWIO (Fig. 1), which contributes to approximately 10-12% of the worldwide cyclonic activity [14-16], is indeed widely considered as the cyclonic basin with the highest prevalence of OA interactions [17] due to the unique structure of the thermocline in the Seychelles-Chagos Thermocline Ridge area (55-70°E, 5-15°S) [18,19]. Like most TC basins, the SWIO includes many fragile countries, whose economic development, infrastructure, as well as food, medicine and water supply chains are regularly impacted by tropical cyclones.

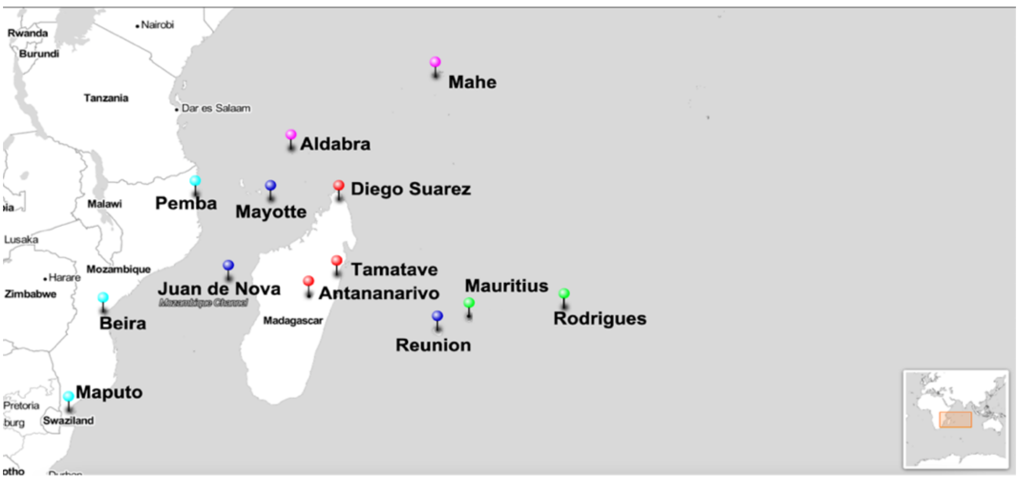

Figure 1: Map of the SWIO TC basin ([30-90°E, 0-40°S]). The principal locations discussed in the paper are indicated by dark blue (France), light blue (Mozambique), green (Mauritius), red (Madagascar) and pink (Seychelles) circles.

In very recent years, countries bordering the Mozambique Channel (MC) have indeed been struck by a series of extremely intense and devastating events, whose economic impact will be felt for many years to come. Heavy rains associated with TC DINEO (2017) have caused 700,000 refugees and tens of millions of US$ of damage in Mozambique, while the overall cost of TCs ENAWO (2017) and AVA (2018), which affected nearly one million people in Madagascar, was estimated to more than US$ 600 millions (about 7% of Madagascar's average annual gross domestic product). These heavy tolls are, however, out of all proportion to those of TCs IDAÏ (considered by United Nations as the worst natural disaster ever in the MC) and KENNETH (the most intense TC ever reported in the MC [20]), which both made landfall in Mozambique in 2019 [21]. According to the latest economic reports, these two storms have affected a total of nearly 1.7 million people and caused damage and losses estimated at ~US$ 3 billion - plus a further recovery cost estimated at US$ 3.4 billion - by the World Bank and Mozambican officials [22].

Given the colossal impact of TCs on local populations, infrastructures and economic development of many countries in the SWIO basin, the European Union (EU), together with the Regional Council of Reunion Island and the French State, have designed the transdisciplinary research program "REunion NOVative research on cyclonic RISKs" (ReNovRisk), to improve the resilience of SWIO countries to TC hazards and mitigate associated economic vulnerability, damages and risks (e.g., winds, rainfall, landslides, submersion) in inhabited areas. To achieve these objectives, ReNovRisk has been divided into four interlinked research projects, referred to as ReNovRisk-Cyclone, -Erosion, -Impacts and -Transfer, whose overall objectives are described in [23]. The present paper focuses on the Cyclone component of this program, which involves a large international consortium of research institutes, universities and weather services originated from France [e.g., universities of Reunion Island and Toulouse, Centre National de Recherche Scientifique (CNRS), Météo-France, Institut de Physique de Globe de Paris (IPGP), Institut National de l'Information Géographique et Forestière (IGN), Institut Français de Recherche pour l'Exploitation de la MER (IFREMER)], Mozambique [Eduardo Mondlane and Pemba Unilurio universities, Mozambique Weather Service (INAM)], Madagascar (Institut Supérieur de Technologie de Diego Suarez, University of Antananarivo), the Seychelles (Seychelles Meteorological Authority, Seychelles Islands Foundation), Mauritius (Mauritius Oceanography Institute), as well as international institutions such as the European Space Agency (ESA) and WMO, among others.

Through its observing, modelling, climate and outreach components, ReNovRisk-Cyclone (hereafter referred to as RNR-CYC) is aimed at improving the observation and modelling of TCs, as well as to foster regional cooperation and improve public policies adapted to present and future TC risks faced by territories bordering the SWIO. The latter is all the more essential as predicted changes in the coupled OA system due to global warming are likely to generate significant modifications of the cyclonic activity in the coming decades. Consequently, regions that are currently spared or moderately affected by TCs, and that often lack experience-based adaptation strategies, may soon have to face potentially increasing TC-related hazards [24-25]. Such changes include for instance the widening of the tropical belt resulting from ocean warming (e.g., [26-27]), which has already been shown to induce a poleward migration of TC's lifetime maximum intensity (LMI) in both hemispheres [28-31], or significant modifications in TC frequency and/or length of the TC season [32].

This paper is aiming at describing the structure and main objectives of the project RNR-CYC, as well as to present an overview of the main applications and results of its observation component - modelling aspects are presented in more details in the companion paper [33]. This article is organized as follows: Section 2 provides an overview of the four components of RNR-CYC (observation, mesoscale modelling, climate modelling, cooperation and outreach). Section 3 presents the major achievements of RNR-CYC regarding oceanic and atmospheric observations, while Section 4 concludes and discusses new research topics to be investigated past this program.

2. Structuration and objectives of RNR-CYC

The project RNR-CYC focuses on the meteorological and oceanographic impacts of TCs in the SWIO (Fig. 1) at both present and future horizons. It aims, in particular, to better apprehend the impacts of these extreme storms on the main inhabited islands of this oceanic basin by providing innovative modelling and observing products that will also feed the cascade risk analysis tools deployed in the other research component of the global ReNovRisk program [23]. In order to achieve these objectives, RNR-CYC has been divided into 4 components: i) an observation component, to improve both long-term and temporary observations of TCs and their atmospheric and oceanic environments, ii) a mesoscale modelling component, to improve modelling and short-term forecasting of TCs, iii) a climate component, to evaluate the consequences of climate change on the variability and structure of TCs at both local and basin scales, and iv) an outreach component, aimed at improving capacity building in the three aforementioned research areas through strengthening cooperation between SWIO countries. An overview of the structure and objectives of these four components is described hereafter.

2.1 Observing component

The observing component of RNR-CYC is aimed at providing additional observations of TCs and their environment by improving regional and local observing capabilities in the SWIO. It has been built around three complementary approaches:

i) A "conventional" approach, based on the reinforcement of regional ground-based meteorological observation facilities and, in particular, of the water vapor Global Navigation Satellite System (GNSS) observation network operated by the International GNSS Service (IGS). Starting in November 2017, 10 new public observation sites (composed of ground-based GNSS receivers and colocated surface weather stations) have been deployed in Madagascar, Eparses Islands and the Seychelles in the frame of RNR-CYC's sub-program "Indian Ocean GNSS Applications for Meteorology" (IOGA^{4}MET; [34]) to increase the number of tropospheric GNSS measurements (e.g., zenithal delay, integrated water vapor amounts) and positioning data throughout the western part of the basin (see Section

3.2.3). The first analysis of GNSS-derived observations collected during RNR-CYC have already demonstrated the benefit of these new permanent stations to investigate the water vapor cycle at diurnal to inter-annual time scales [35], but also to provide new and continuous observations to investigate the dynamics of the Earth's crust in this particularly active part of the world [34,36].

ii) An "experimental" approach, based on the temporary collection of atmospheric and oceanic observations at various locations in the basin. For this purpose, several atmospheric and oceanographic field campaigns have been organized throughout the 3 ½ years of RNR-CYC with the goal to provide novel datasets to evaluate numerical model simulations performed in the frame of the project. The main achievements include:

- A 3-year satellite acquisition campaign (2017-2020), setup in collaboration with ESA and IFREMER, to collect high-resolution (1 km) observations of surface winds and sea roughness from spaceborne synthetic aperture radars (SAR) deployed onboard the satellites Sentinel 1A/1B of the European Earth Observation Program Copernicus[1] (see Section 3.2.4).
- A regional field campaign, organized from late January to early April 2019, to investigate atmospheric and oceanic environmental conditions prevailing in the vicinity of TCs during the 2018-2019 TC season. During this 2 ½ month period, a regional radiosounding network, allowing for the collection of nearly 500 soundings, was deployed in Mayotte (France), Toamasina (Madagascar) and Maputo (Mozambique) to both sample the atmospheric environment of TC and train students and academics in experimental meteorology (see Section 2.4).
- The deployment of two ocean gliders from Reunion Island to sample the vertical properties of the upper ocean layers in the Mascarene Archipelago (see Section 3.1.4).
- The deployment of an unmanned airborne system (UAS), equipped with aerosol, turbulence, sea state, and meteorological sensors to measure OA fluxes and aerosol concentrations in the vicinity of Reunion Island (see Section 3.2.1).
- The organization of several local observation campaigns to sample sea swell properties during austral winters and summers using acoustic Doppler current profilers (ADCP) and wave gauges deployed near-shore Reunion Island (see Section 3.1.1).

iii) An "exploratory" approach, based on the deployment and evaluation of innovative methods to collect oceanographic observations. A particularly original approach, based on the biologging technology, has been evaluated for 2 years to collect data from sea turtles (ST) equipped with dedicated ARGOS environmental tags in the frame of RNR-CYC's subprogram "Sea Turtle for Ocean Research and Monitoring" (STORM, see Section 3.1.3). Another original approach, based on the previous work of [37-39], has also been further investigated to quantify extreme swell phenomena from microseismic noise measurements recorded by ground seismometers (see Section 3.1.2). The preliminary

[1] https://www.copernicus.eu/fr

assessment of terrestrial seismic observations collected in Reunion Island against oceanographic records and offshore wave model data, have demonstrated that land-based seismic stations could be particularly useful to observe both austral [40] and cyclonic swell [41] (this special issue).

2.2 Modelling component

Protecting life and property requires a precise estimate of the environmental changes associated with the passage of TCs in the vicinity of inhabited areas. The challenge in the face of the cyclonic threat is to simultaneously predict the track and intensity of the storms, but also the consequences resulting from their landfall, or transit near inhabited areas. Hence, damages caused to a given territory, which are essentially related to rainfall intensity, wind strength and sea state (e.g., swell), could significantly differ depending on whether it is affected by a tropical storm (TS), a monsoon depression or a more or less intense TC. To this end, many operational meteorological services and research centers concerned with TC hazards have made considerable efforts to develop deterministic and ensemble coupled NWP systems providing high spatial resolution forecasts in all TC basins (e.g., [42-46]).

Improving TC forecasting first and foremost implies a proper representation of the interactions between the storm and the ocean, and vice versa [47]. During the propagation of a TC over an oceanic area, mixing caused by surface winds usually induces a significant drop in surface temperature [48-49] that strongly reduces surface enthalpy and heat fluxes (e.g., [50,51]). These air-sea fluxes can also be significantly impacted by waves, which redistribute momentum in the near-surface layer and modify the enthalpy fluxes through the emission of sea spray [52-57]. In this regard, new parameterizations reproducing the impact of marine aerosols on turbulent heat exchanges have been proposed and validated in recent years (e.g., [58-59]), but are yet to be implemented in atmospheric models to thoroughly evaluate their impact on TC behavior.

Because radiative cooling (e.g., [60,61]), evaporation (e.g., [62,63])) and latent heat release (e.g., [64]) have long been recognized to play a key role in the development and intensification of tropical cyclones, a particular attention must also be paid to microphysical schemes implemented in NWP systems. These schemes must, in particular, allow for an efficient representation of the radiative cooling at the top of the storms (which is a constraining criterion of TC intensity) and of the vertical distribution of latent heat (which represents the main source of energy of TCs). They should thus also be able to realistically take into account the role of atmospheric aerosols, that (indirectly) affect the radiation balance by impacting on the radiative and precipitating properties of the clouds. Improving TC forecasting therefore also implies the development of coupled aerosol-microphysical-radiation schemes to be integrated in fully coupled ocean-wave-atmosphere (OWA) models.

An important objective of RNR-CYC was to develop high-resolution OWA and OA modelling systems capable of representing as exhaustively as possible the multitude of physical interactions that control the variations of intensity of TCs, as well as their impacts (wind, rain, swell) at the scale of SWIO territories. The main modelling developments made in the frame of this project can be found in [11, 64, 65 (this volume)] and in the companion paper [33].

2.3 Climate component

Evaluating the impact of climate change on the frequency and intensity of tropical cyclones is considered as one of the top 5 issues of concern by the IPCC. Currently, regional and global climate models make it possible to identify the preferred areas of cyclogenesis and occurrence of tropical low-pressure systems at the basin scale, but cannot be effectively relied upon yet to investigate potential changes in their structure and intensification mechanisms. While it is now widely accepted that the global increase of sea surface temperatures in tropical areas will be a favorable element for TC development, it is not clear how other ingredients involved in their formation and intensification will evolve in the future. In this regard, another important objective of RNR-CYC was to evaluate the global evolution of cyclonic activity in the SWIO, but also to investigate potential structural and intensity changes of TCs resulting from the ongoing modification of their oceanic and atmospheric environments.

The modelling strategy was based on two complementary approaches, allowing to both estimate the evolution of cyclonic activity at the basin scale (i.e., changes in trajectory, intensity and frequency of TCs at different time scales), and to assess potential structural changes and impacts of TCs at the local scale. This strategy relies on the exploitation of unprecedented high-resolution global climate simulations [32], as well as of mesoscale coupled simulations to estimate the impact of climate change on the intensity, behavior and consequences of cyclones at the scale of a given territory. Examples of results obtained from such high-resolution model runs are discussed in [33,67] (both in this special edition).

2.4 Regional cooperation

Another important objective of RNR-CYC is to provide enhanced tools and knowledge to countries of the SWIO facing cyclonic hazards. Responding to this strong societal issue requires a better structuring of the regional scientific community, as well as a significant reinforcement of the cooperation between countries bordering the SWIO basin. While regional collaboration already exists through WMO's regional structures [e.g., Tropical cyclone Programme[2], Reunion Island's Regional Specialized Meteorological Center (RSMC La Réunion[3])] and the Indian Ocean Committee[4], interactions remain essentially focused on operational and technical applications and only modestly promote research development in this area.

---

[2] https://public.wmo.int/en/our-mandate/focus-areas/natural-hazards-and-disaster-risk-reduction/tropical-cyclones

[3] http://www.meteo.fr/temps/domtom/La_Reunion/webcmrs9.0/anglais/index.html

[4] https://www.commissionoceanindien.org/

One of the strengths of RNR-CYC consists in the implementation of a partnership involving many regional research institutes, universities and meteorological services that agreed to pool their resources and expertise to strengthen the resilience to TC hazards and develop public policies better adapted to the risks faced by SWIO territories. RNR-CYC is thus a fundamentally collaborative project that is not only based on a large sharing of data and experiences, but also on training programs and capacity building initiatives in the fields of observation and forecasting. These actions include for instance the organization of forecasting training sessions at RSMC La Réunion, of training courses in climatology and climate change, as well as numerous co-supervised MSc internships based on the analysis of experimental measurements collected in the project.

The project's field phase, which involved nearly a hundred participants from January to April 2019, was also an opportunity for many students and researchers to initiate themselves to the technique of atmospheric radiosounding (RS). During this 2 ½ month campaign ~500 radiosoundings have been performed from three experimental sites specifically deployed for this occasion in Maputo (INAM's headquarters, Mozambique), Mayotte (Météo-France weather center, France) and Toamasina (Toamasina international airport, Madagascar). On this occasion nearly 60 students and academics from Antananarivo (Madagascar) and Eduardo Mondlane (Mozambique) universities came to Toamasina and Maputo to make RS, while many senior forecasters of INAM and Météo-France Mayotte had, for the first time, the opportunity to operate and familiarize themselves with a RS station (Fig. 2).

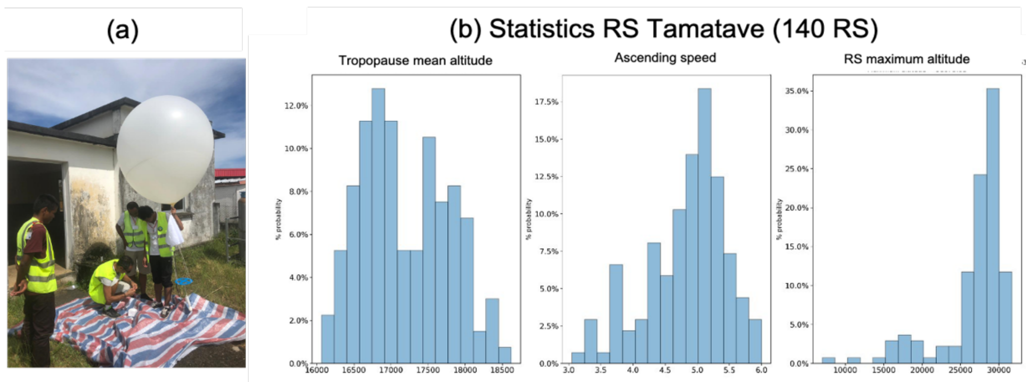

Figure 2: The Toamasina (Madagascar) radiosounding campaign. (a) Training of students from Antananarivo university at Toamasina airport. (b) Statistical analysis of the 140 RS made in Toamasina: mean altitude of the tropopause, ascending speed and maximum RS altitude.

The involvement of the French consular services in the project has also made it possible to communicate widely to the general public, the scientific community and the media in Mozambique, Madagascar and the Seychelles on the issues of adaptation to climate change and natural hazards. As will be seen in Section 4, these regional collaborations will continue for many years to come through several new research projects initiated from RNR-CYC.

3. Results

3.1 Oceanic observations

3.1.1 In-situ swell observations

One of the main objectives of RNR-CYC is to assess the impact of tropical cyclones on land, including possible submersion resulting from cyclonic swell surge along coastlines. In many tropical islands, the latter are bordered by coral reefs that can serve as a defense against flooding. These reef systems, particularly fringing reefs, protect the coastline by acting as low-pass filters that can reduce the energy of wave flows reaching the coast by up to 98% in the gravitational part of the wave spectrum [68]. The physical processes underlying coral reef coastal protection consist of a complex combination of incident waves, tides and wind induced surges [69-71].

Ocean wave energy is concentrated in the gravitational frequency band of the wave spectrum, generally between 0.04 Hz and 0.25 Hz. These gravitational waves (GW) are the main drivers of the hydrodynamics of reef systems, as well as of beaching, runup and submersion. During and after breaking at the edge of reef systems, GW are dissipated while low frequency waves (infragravity waves (0.004 < IG (Hz) < 0.04) and very low frequency waves (0.001 < VLF (Hz) < 0.004) propagate to the shore. Previous analyses of these propagation and transformation processes across various coral reefs have shown that wave dynamics could vary considerably depending on the characteristics and location of reef systems [71,72].

In order to both quantify the physical processes linked to severe sea states and assess the protective role of reef systems, a cross-shore transect, composed of bottom fixed wave gauges and ADCPs, was deployed in Reunion Island from February to April in 2019 and 2020. Instruments were installed at the fringing reef of "Trou d'Eau", located along the west coast of the island (Fig. 3a). At the near-shore site, reef-base (RS) and reef-flat (RF) stations were deployed through the fringing reef along a cross-shore transect. The RS station was installed at the base of the reef slope at an average depth of 12 m, while three RF stations (RF1, RF2 and RF3 in Fig. 3a) were aligned on the flat reef inside the lagoon at the depth of 1 m (Figs. 3b and 3c). RS and RF stations were all equipped with synchronized ocean sensor system instrument (OSSI) wave gauges allowing to continuously record pressure at a sampling frequency of 10 Hz. The RS station also featured an upward looking Nortek AQuadopp (AQP) profiler configured to measure current profiles every 20 min, with a 2 Hz hourly burst mode to record wave parameters. In 2020, an ADCP (RDI Sentinel V100) was also deployed at an ocean offshore (OC) site at a depth of 45 m. This instrument was configured to record incident wave parameters from hourly bursts of 2100 samples at 2 Hz, and current profiles from the bottom to the surface.

Observations collected at the offshore stations OC and RS were relied upon to describe and quantify the main properties (height, period and direction) of the waves impinging on the reef in the GW frequency band (wave periods ranging from 4 to 25 s), while data gathered at RF stations were used to investigate wave propagation (from outside the lagoon to the shore) and transformation (across the fringing reef). Observations collected at the OC and RS stations were processed with the RDI software "Velocity" and the PUV method [73], respectively. All OSSI pressure data were corrected from atmospheric mean sea level pressure data recorded at the surface weather station of "La Rivière Des Galets" (located 20 km northward of the experimental site, RDG on Fig. 3a) and non-hydrostatic pressure following the linear wave theory [74].

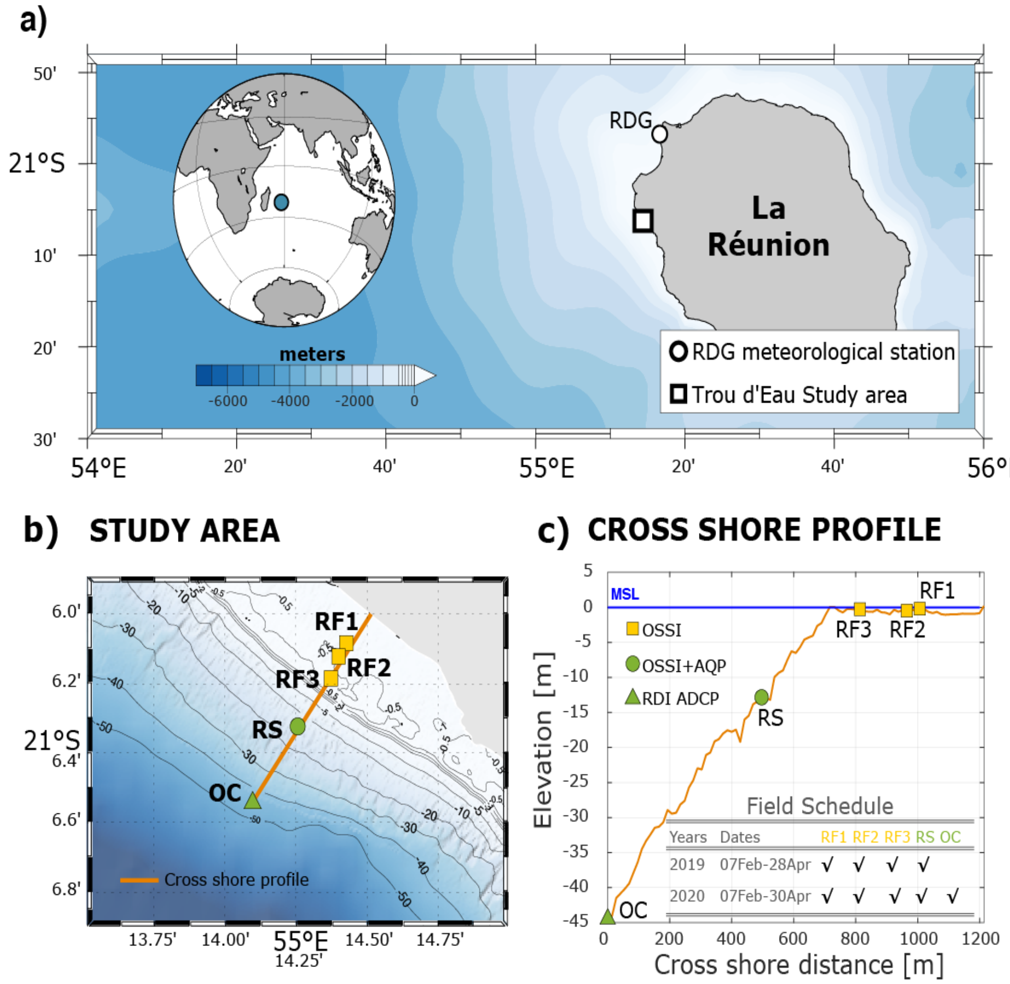

Figure 3: Overview of the experimental setup deployed in "Trou d'Eau" (Reunion Island) in February-April 2019 and 2020. (a) Coastal study area, (b-c) details of the cross-shore transect instrumented during the experiments. The stations are labeled OC for ocean offshore, RS for reef-slope and RF for reef-flat. In (c) labels OSSI, AQP and RDI ADCP correspond to wave gauges, Nortek AQuadopp current Profiler, and RDI ADCP current profiler, respectively. Instrument deployment dates are indicated in (c).

The mean surface elevation is computed from a 20-min moving average of the signal, while the wave spectrum and average wave parameters is obtained through the application of a fast Fourier transform (FFT). The latter was applied over 4096 data for incident gravity waves band or swells (0.04 < SW < 0.25 Hz) and 32768 data for infragravity (0.004 < IG < 0.04 Hz) and very low frequency (0.001 < VLF < 0.004 Hz) bands. Since the recorded signal is not perfectly periodic, a Hamming window, leading to zero value at the edges, is also applied to mitigate artifacts resulting from leakage issues. To avoid resulting loss of information at the edges, a 30-minute (resp. 3 hours) time average is then performed for the incident (resp. IG and VLF) bands. Time series of power spectra density deduced from data collected in 2019 along the cross-shore transect are shown in Figure 4, together with associated mean power spectra at each station.

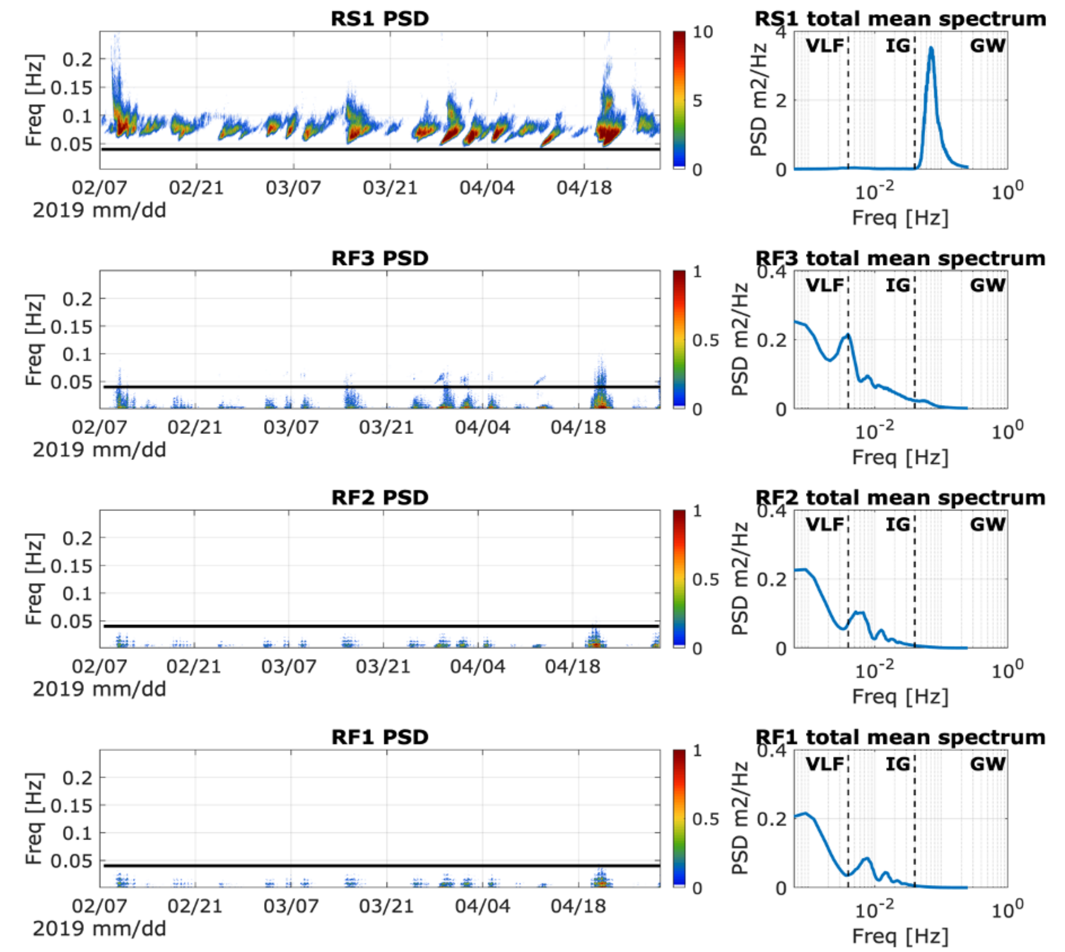

Figure 4: Spectral wave characteristics observed along the instrumental transect presented Fig. 3b. The plots are organized in the shoreward direction from the top to the bottom (reef slope RS1 station on top and reef flat station RF1 closest to the shore on bottom). The left panels show the temporal variation of the wave spectrum recorded at each station from February to April 2019. The black solid line indicates the frequency cut at 0.04 Hz between the gravity frequency band (GW) and the infragravity (IG) frequency band. The right panels show the mean power spectral density for each station averaged over the whole period, with the frequencies band GW, IG and VLF (for very low frequency) indicated.

Measurements collected at the reef slope station RS clearly show that the wave energy spectrum is concentrated in the gravity band, with an averaged peak period of 13.5 s over the whole period. After breaking at the reef crest, most of this energy is dissipated (by breaking and/or by friction on the reef bottom), while the remaining energy (in IG and VLF bands) is transferred inside the reef system. For the two strong wave events respectively observed in February (likely associated with TC GELENA to the north of Reunion Island) and April 2019 (austral swell event), the total wave energy reduction between the reef slope station RS and the adjacent reef flat station RF3 reaches 98%, a value in good agreement with previous meta-analyses [68]. Within the reef, the transfer of the remaining energy between the 3 stations is nevertheless slightly different for these two events. In February (TC event), the wave energy reduction reaches 64% from RF3 to RF2 and 2% from RF2 to RF1, but in April (austral swell event), the wave energy reduction was only 47% from RF3 to RF2 and 15% from RF2 to RF1. As the main difference between these two events is the period of the incident waves (11.8 s for the TC-related event and 16 s for the austral swell event), this result suggests that the generation and propagation of IG waves inside the reef might be less important for short waves, induced by the wind, than for longer-period swells. This shoreward propagation with less energy reduction is also noticeable in the average spectra, which show a small translation of the peak frequency toward higher frequencies in the IG band, between the RF2 and RF1 station, and reduction of the peak amplitude.

The preliminary analysis of these data shows that Reunion Island's fringing reef plays a strong role in protecting the shore against incident waves. Further investigations will be conducted in order to thoroughly investigate the physical processes and the role of both reef topography and roughness on the dynamics of IG waves. This includes for instance the impact of shoreward propagating IG waves on onshore suspended-sediment transport [75], and the relationship between long wave propagation (and transformation) across the reef and sea water level above the reef - the remaining long waves propagating through the reef have been shown to increase the back-reef set-up and beach runup, which could lead to increased coastal erosion during extreme events such as tropical cyclones or strong storms [76,77].

3.1.2 Ground-based swell observations

The global monitoring of swell activity induced by tropical storms (TS) and TCs is of major interest to quantify the risk associated with extreme swells, but also to validate numerical models used to predict ocean activity. Direct swell observations such as those presented in the previous section are, however, strongly limited by the low number of oceanographic sensors available in this area, as well as by their deployment (and servicing) costs and their vulnerability during tropical cyclones. These limitations have motivated the use of indirect observations as alternative and complementary observables to quantify the swell parameters. In this regard, the analysis of wave-induced seismic noise is known to be an interesting substitute for monitoring ocean activity and has been proven to be particularly relevant for assessing the impact of waves on coastal environments (e.g., [38]). The possibility to derive swell measurements from the seismic noise generated by ocean swell, and transmitted to the solid earth as seismic waves recorded by terrestrial seismological instruments (e.g., [78]), is discussed hereafter from data collected in RNR-CYC.

Microseisms recorded by seismic stations worldwide are known to be generated by ocean gravity waves (e.g., [79]). Seismic energy spectra at terrestrial seismic stations show two clear peaks in separate frequency bands that characterize two kinds of seismic noise. These peaks, known as primary and secondary microseisms (hereafter named PM and SM, respectively), are widely accepted to represent different physical processes involving local or distant sources of ocean wave activity [80]. Primary microseisms (PM) are mostly visible at coastal and island stations and are assumed to be generated by direct interaction of swell-induced pressure variation with the coastal seafloor [81-83]. Because PM noise has the same periods as the ocean swell (i.e., between 8 and 20 s), analyzing microseismic noise in this frequency band is, therefore, a powerful way to characterize the local impact of swell approaching the shore. On the other hand, SM noise is generally generated in the deep oceans and at larger distances from coastal areas [37, 84-86]. It dominates seismic noise at both continental and oceanic stations and exhibits a large peak at half the period of ocean waves (i.e., between 3 and 10 s), which is assumed to be generated by the interference of swells of similar periods travelling in opposite directions [79]. These interferences create stationary waves whose pressure fluctuations on the seafloor induce seismic surface waves travelling horizontally within the solid crust.

In the Indian Ocean, most remote sources of seismic noise are located in the southernmost part of the Austral Ocean basin and are associated with storm systems moving around Antarctica [84, 87, 88]. Some noise sources may also develop at tropical latitudes in association with tropical cyclones [41] (this special issue). Recent seismic deployments on the ocean floor allowed to make *in situ* observations of SM underneath TCs in the neighborhood of Reunion Island [37] and confirmed the possibility to track TC and TS from the ocean bottom. Although SM are generally created by distant storms, they can also be generated by coastal reflection of waves if incident and reflected waves propagate in opposite directions (e.g., [89,90]). In this latter case, the incoming swell may interfere with its reflected swell, resulting in the generation of standing waves close to coastal areas that oscillate at twice the frequency of the propagating wave [91]. Some seismic observations also suggest that local and distant sources of noise in the SM frequency peak, usually referred to as Long Period Double Frequency (LPDF) or Long Period Secondary Microseisms (LPSM) in the literature, may coexist (e.g., [39,92,93]).

Previous seismic analyses conducted in the Pacific and Indian Oceans have already demonstrated that several swell parameters can be derived from the seismic data. This includes (i) the swell peak period *Tp,* derived from the dominant frequency of the PM and SM using the power spectral density analysis of the seismic records, (ii) the local or distant wave significant height *Hs* (in the case of the PM or SM band, respectively), obtained by measuring the microseism amplitudes through hourly Root Mean Square (*RMS*), and (iii) the wave peak direction *Dp* for the case of the PM band, or the source direction in the case of the SM or LPSM bands, which can both be deduced from the polarization analysis of the three seismic data component, to determine the dominant direction and strength of the recorded microseismic noise.

To illustrate this innovative approach, we present below the analysis of seismic observations collected during the tropical storm (TS) ELIAKIM that developed in March 2018. This storm is interesting because it had clear signatures in the data, despite not reaching tropical cyclone intensity, and developed at a large distance from Reunion Island, thus allowing to demonstrate the potential of the method in quantifying remote systems. As mapped on Figure 5a, TS ELIAKIM started as a depression located NE of Madagascar on 13 March 2018. It then intensified to a tropical storm on 14 March and to a strong tropical storm on 15 and 16 March while approaching the eastern coast of Madagascar, where it made landfall on 17 March. TS ELIAKIM continued its southward motion and returned back over the ocean on 18 March. After a final burst on 19 March, the storm definitely collapsed on 20 March, while entering its extratropical transition phase.

The following analysis was performed from data recorded by seismic stations of the permanent seismic network of the Piton de la Fournaise Volcano Observatory (OVPF, seismic code PF, red triangles on Fig. 5b) and from a temporary seismic network deployed in the frame of the RNR program (code ZF, blue triangles on Fig. 5b). Seismic data are compared with swell parameters issued from the *WaveWatch3* (WW3) model [94,95] at nodes surrounding the island from the global wave model hindcast [96], indicated by stars on Fig. 5b.

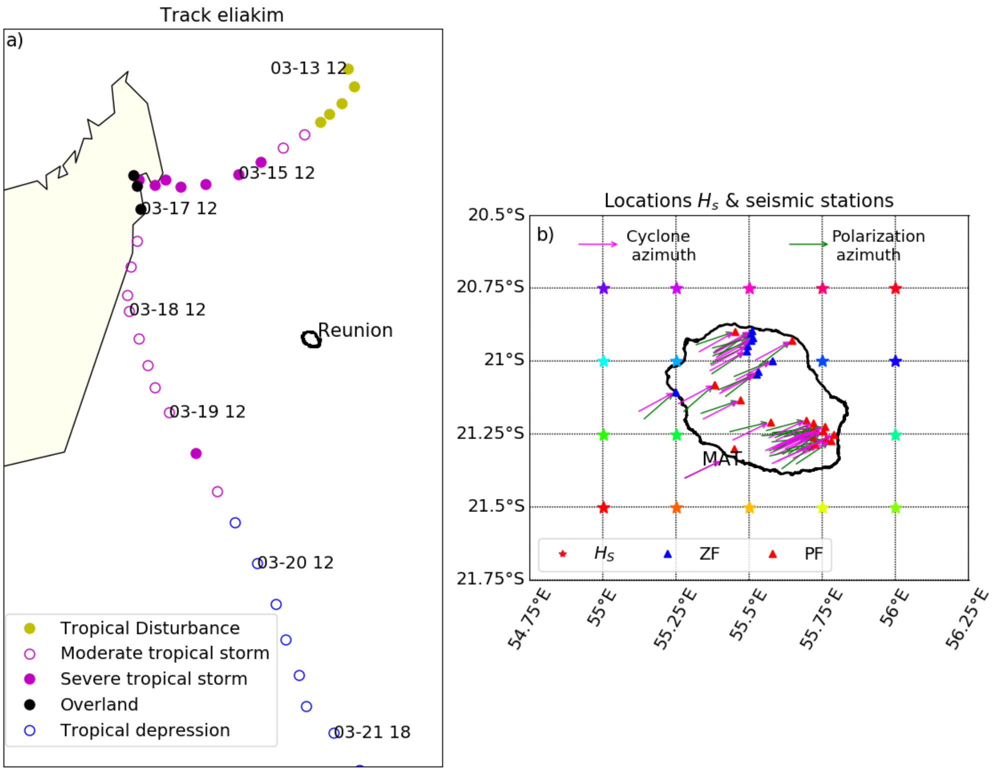

Figure 5: a) Track of TS ELIAKIM as derived from RSMC La Réunion best-track data. The colored circles indicate the position and intensity of the storm every 6 hours. b) Locations of the seismic stations (blue triangle, temporary ZF network, and red triangle, permanent PF stations) and WaveWatch3 nodes [96] surrounding the island, where wave height Hs (colored stars) is extracted. Vectors indicate the average azimuth on March 19, 2018, obtained from the polarization analysis in the SM frequency band (green) and computed from the storm track and the RER seismic station (pink).

The seismological energy content of the vertical ground displacement of station MAT (Fig. 5b) is shown in the spectrogram of Figure 6a. It displays the temporal variation of the Power Spectral Density (PSD) during the period March 10 to 25, 2018 over the frequency band of the ocean activity (0.05-0.5 Hz, i.e., 20-2 s periods). Superimposed to the spectrogram is the distance curve of the storm center to Reunion Island (dashed line), together with the storm intensity curve (black line indicating the mean wind speed and the colored dots the storm classification, as Fig. 5a). The seismic energy at this station shows good correlation with the storm intensity, despite its large distance, varying from 500 to 1500 km. One can see two pulses of energy with the maximum at a frequency range of 0.1-0.3 Hz, i.e., in the SM band, culminating on March 16 and 19, which correspond to the two maximum storm intensity. Below 0.1 Hz, i.e., in the PM band, the PSD still displays clear energy increasing during the two storm peaks.

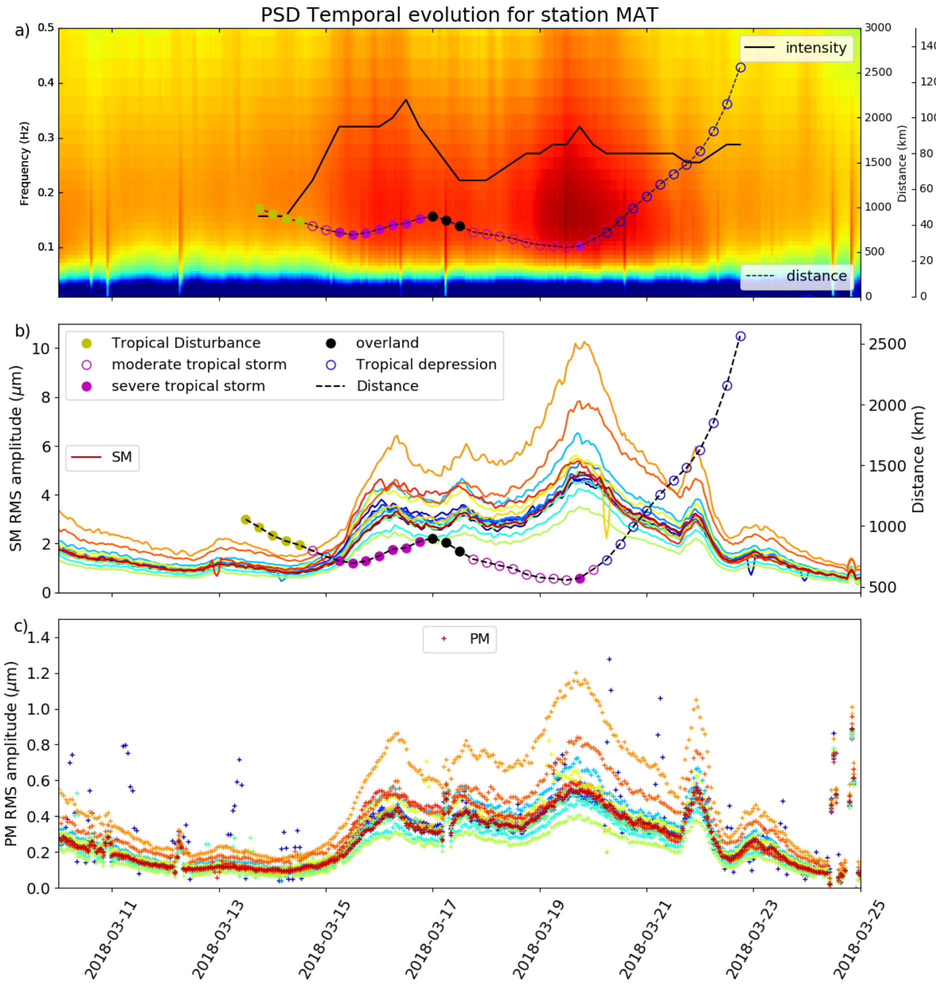

Figure 6: Temporal variation of the microseismic noise recorded during TS ELIAKIM. a) Spectrogram at seismic station MAT (see location in Fig. 5b) between March 10-25 and up to 0.5 Hz, together with the storm intensity (continuous black line) and distance between the storm center and the seismic station (dashed black line). The colored circles indicate the intensity of the storm every 6 hours, as on Fig. 5a). b) Secondary microseisms RMS amplitude variations measured at the island seismic stations (left axis, in micrometers), together with the distance between the storm and seismic station (right axis, in km). c) PM RMS amplitude variations (left axis) at Reunion Island seismic stations.

The hourly RMS amplitudes of the seismic noise recorded at the various seismic stations on the island are shown in Figures 6b and 6c, for both the SM and the PM bands, respectively. Note that the vertical axes are different and that the SM amplitude is almost one order of magnitude larger than the PM. The 21 seismic stations analyzed over Reunion island display similar variation patterns. This indicates that this noise is not a purely local source, the storm acting as a distant SM source, or that the source - if local - is larger than the size of the island, which is the case for the swell generating the PM. One can however notice some variability in the RMS amplitudes from station to station. Interestingly, the station order for the noise amplitude is roughly the same in the two SM and PM bands. This suggests that the actual amplitude of microseisms depends on local site effects such as the installation, the coupling of the seismic sensor with the ground, the nature of the bedrock and the attenuation around the station.

The RMS peaks at seismic station MAT (Fig. 6b) are observed on 16 and 19 March. This period corresponds to that of TS ELIAKIM maximum intensity and to the local variation of the swell height, as visible on *Hs* data issued from WW3 model at various points around Reunion island (Fig. 7). The maximum *Hs* observed on 19 March (corresponding to the nodes at the longitude of 55°E) interacted with the local bathymetry slightly later, which explains the small delay with the PM. Note that a small peak is also observed on 21 March in both SM and PM data. This peak with dominating energy at period ~10s likely originates from a distant source (as already observed for the storm FERNANDO by [40] and does not appear to be related to any local swell activity increase.

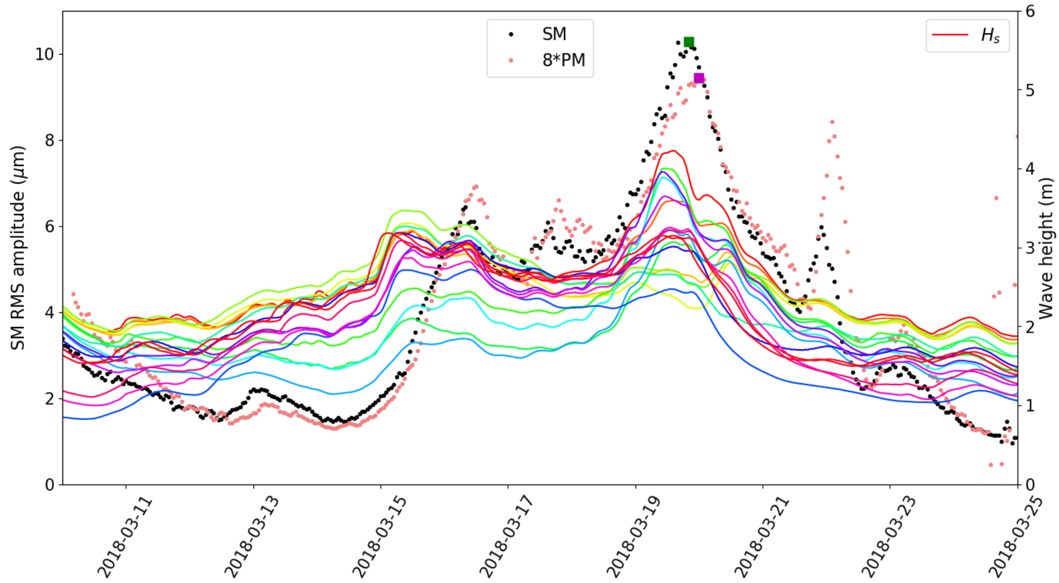

Figure 7: Seismic and swell amplitudes recorded during TS ELIAKIM in March 2018. SM (black dots) and PM (pink dots) RMS amplitude at seismic station MAT (see location Fig. 5b) versus the significant wave heights (*Hs*) at different nodes around La Réunion (colored lines). Note that the amplitude of the PM is multiplied by 8 to reach about the same scale as the SM. The green and magenta dots indicate the maximum SM and PM, respectively, showing a delay of 4 hours between the two. The significant waves heights *Hs* extracted at the various model nodes around the island (Fig. 5b) are plotted in continuous colored lines with the same color codes as the stars in Fig. 5b.

If one accepts that the SM is generated in the vicinity of the storm center and that the PM is generated in coastal areas closer to the seismic stations, one should observe a delay between the two curves. Such delay was previously observed for austral swells generated by distant storms [40] and proposed as a precursor for predicting coastal submersion in Reunion island. In the present case, considering the involved distances (TS ELIAKIM is located ~800 km of the coast of Reunion Island on 16 March, and 500 km on 19 March) and the involved velocities (3 km s^{-1} for the surface waves carrying the SM signal, and ~50 km h^{-1} for the long period waves at the surface of the ocean), one should expect a delay >10 h for each peak. However, Figure 7 shows a delay of only ~4h between the SM and PM. This may indicate that the SM is not generated at the storm center, but likely closer to the island. Alternatively, it may also indicate a slow wind-wave growth that may take from a few hours to few days [97]. The swell–noise amplitude correlation can be used to build a transfer function to translate the amplitude of the seismic noise in terms of swell height. Although such relation is station-related, and therefore not universal, it was nevertheless shown to provide particularly good results for strong swell events (e.g., [40,41,81]).

The recordings of the three components of the ground motion also make the seismic noise a vectorial observation for measuring the direction and strength of the signal polarization. In the case of the SM band, the polarization is expected to point towards the noise source, i.e., the storm center, whereas it should indicate the very local swell propagation direction in the case of the PM. In this PM case, some angle may therefore exist between the swell propagation direction at a large distance offshore and the swell at the coast, due to the interaction between the swell and the dipping shallow bathymetry near the coast and thus, the swell refraction. In the case of TS ELIAKIM, the polarization was measured on an hourly basis in the SM frequency band. Figure 5b displays the average polarization recorded on 19 March at the various land seismic stations in the 0.1-0.33 Hz frequency band (pink) that can be compared to the azimuth computed from the storm center position. This map illustrates a very homogeneous orientation of the noise polarization across the island, pointing to the SW (toward the storm center location on that date) confirming that the SM originates in the vicinity of the storm center.

These results confirm that seismic noise may provide a useful proxy to quantify the swell parameters. In the PM band (10-20s period), the seismic noise amplitude allows for a robust quantification of the swell height *Hs* through a transfer function, the spectrogram allows deciphering the swell dominant period *Tp*, and the polarization analysis allows retrieving the local swell direction *Dp*. In the SM band (3-10s period), the amplitude reveals the storm strength and the polarization indicates the storm azimuth. Terrestrial seismic stations therefore provide alternative and complementary observables of both TC and ocean activities. In some cases, the availability of several decades of seismic archives may also provide new opportunities to derive cyclone climatologies [41] (this volume).

3.1.3 Biologging observations

Observing the vertical structure of the ocean is essential to improve knowledge of both the coupled OA system and marine ecosystems. In this regard, an increasingly common alternative to gather high-resolution hydrographic profiles in the world's oceans is to rely on animal-borne sensors (a.k.a. biologging) to collect in-situ observations in remote and under-instrumented areas. Compared to conventional oceanographic in-situ observation approaches (e.g., gliders, ARGO drifter, buoys, research cruises), animal-borne electronic ARGOS tags are relatively inexpensive to operate and can be deployed in remote areas with limited human resources. As this approach offers all countries the possibility to actively contribute to the collection of ocean observations, biologging is expected to grow considerably in the future. The recent decision, in August 2020, of the Global Ocean Observing System (GOOS)'s Executive Committee to create a new observing network exclusively dedicated to animal-borne ocean sensors ("ANIBOS") is definitely in line with this perspective and clearly attests of the immense potential of this approach.

The potential of biologging for sampling the thermal structure of the tropical Indian Ocean was evaluated in the frame of RNR-CYC's sub-program "*Sea Turtle for Ocean Research and Monitoring*" *(STORM).* The latter was initiated in January 2019 by Reunion's University and Reunion Island's Sea-Turtle Observatory (Kelonia) with the goal to monitor in near real-time, and at high spatial (<100m) and temporal (5′) resolutions, the state of the tropical Indian Ocean down to several hundred meters below the surface**.** As of March 2021, 22 animals have been equipped with Temperature-Depth (TD) ARGOS tags before their release from Reunion Island (Fig. 8). Note that all these animals were accidentally captured in fisherman's net in the vicinity of Reunion Island and brought back to Kelonia's care center for being healed and rehabilitated.

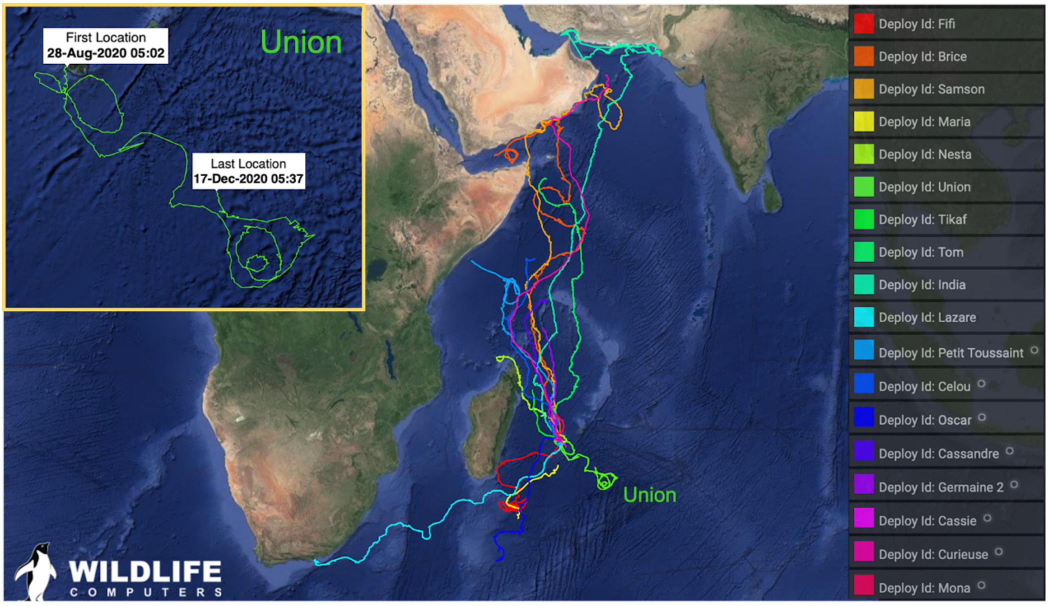

Figure 8: Trajectories and names of the 18 loggerheads and Olive Ridley STs equipped with Wildlife Computers SPLASH10 tags released from Reunion's Island as of 10 March 2021. Circles next to the ST names on the right-hand side indicate active tags as of 20 March 2021. The insert on the left-hand side shows a zoomed view of ST Union trajectory between 28 August and 17 December 2020. Four additional animals, equipped with LOTEK Kiwisat tags, were also released from Reunion island in 2019 (not shown).

During this experiment, two species of late juveniles and sub-adult sea turtles (loggerhead and Olive Ridley) were equipped with Argos TD tags. While some of the animal stay in their pelagic habitats, some loggerheads had also begun their first breeding migration to the Oman Gulf, thus permitting to collect data both in tropical areas, from loggerheads, and subtropical areas, from Olive Ridley (Fig. 8). ST released from Reunion Island principally evolve at (or slightly below) the surface (~50% of the time) and near the bottom of the ocean mixed layer (OML, ~25% of the time). They were found to dive up to 100 times a day, sometimes up to 350m, allowing to collect numerous hydrographic profiles within and far below the OML [9]. The analysis of data collected during the first year of this experiment have confirmed the great potential of this approach for sampling the vertical structure of the ocean, validating ocean models and spaceborne sensors, as well as to investigate the intraseasonal variability of the tropical Indian Ocean [9].

Sea turtles are known to generally evolve in rings and frontal areas in between, and often travel by moving from one ring to another (e.g., [98]). These rings and eddies are numerous in the Mozambique Channel [99-100], but less common in the open Indian Ocean, which may explain which STs released from Reunion Island generally tend to follow a straight trajectory (Fig. 8) - another explanation (currently under investigation) is that STs rarely feed during their reproductive migration so as to reach their breeding areas as fast as possible. According to its circular trajectories, one can however hypothesize that ST Union (Olive Ridley), which evolved SE of Reunion Island in late 2020, often travelled in oceanic gyres and eddies (Fig. 8).

The surface current analysis of Mercator Ocean's operational model NEMO-PSY4 (a.k.a Glo12, [101]), averaged from 15 October to 15 December, confirm that ST Union indeed evolved in cyclonic and anticyclonic eddies of variable sizes during this period (Fig. 9a). Vertical cross-sections of the ocean temperature field across the center of the main eddy (Figs. 9b and 9c) show strong upwellings at the edges (while downwelling can be observed at the vortex center), resulting in significant temperature gradients at the surface (Fig. 9a). This vertical transport, which brings nutrient-rich waters from the thermocline up to the surface, make of these eddies prime feeding areas for many marine species and are particularly appreciated by sea turtles. Equipping STs with environmental tags is thus an easy and relatively affordable way to sample the properties of these transient mesoscale features (see Section 4). The study of their life cycle and impacts on the dynamics of the ocean will be further investigated in the continuation of the STORM program (se Section 4).

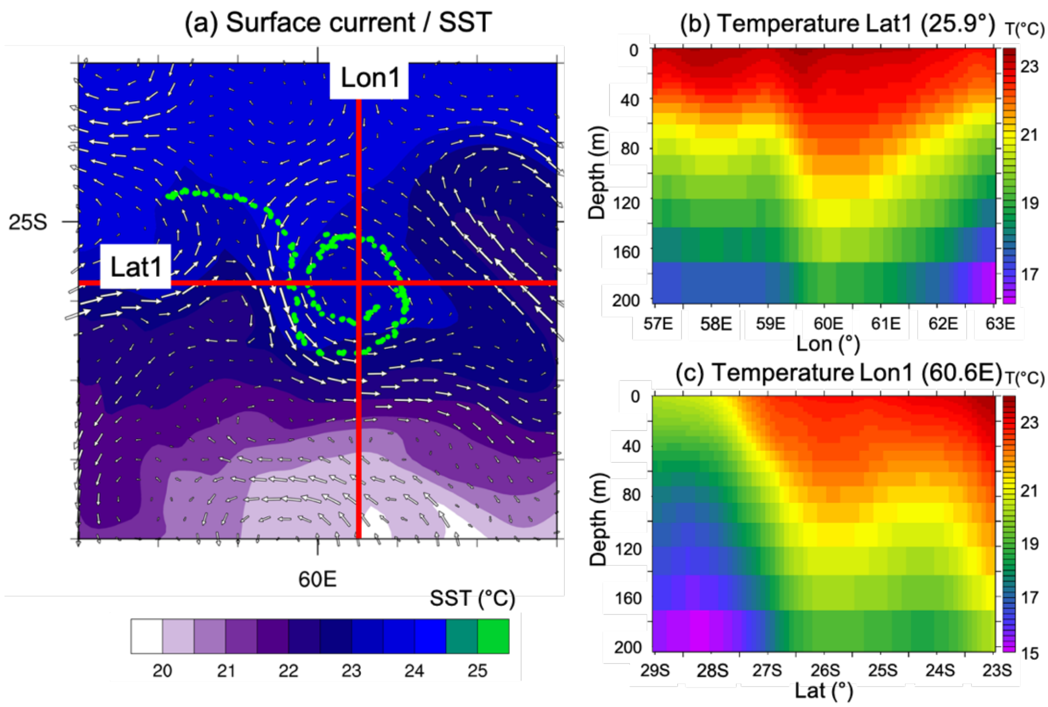

Figure 9: GLO12 model analyses in the area of evolution of ST Union averaged from 15 October to 15 December 2020. (a) surface currents and sea surface temperature superimposed on ST Union track over the 2-month period (green dots), (b-c) vertical cross-sections of ocean temperature through the center of the main vortex travelled by ST Union.

During this experiment, three sea turtles have also been caught in the immediate vicinity of tropical cyclones during the TC seasons 2018-2019 and 2019-2020: ST Brice, which evolved in the vicinity of TC KENNETH (April 2019) during its cyclogenesis (Fig. 10a), and STs India and Tom, which were trapped in TC HEROLD (March 2020) during its intensification phase (Fig. 10b). Because spaceborne oceanic observations are generally unavailable under cloudy conditions, data collected by these animals represent a fantastic opportunity to also investigate the impact of TCs on the surface and subsurface structure of the ocean.

Sea surface temperature data collected by ST India in TC HEROLD from 14 to 20 March 2020 are shown in Figure 10c. During these six days, the animal remained trapped in the immediate vicinity of the storm center (~ 30 km from the TC eye) and only moved by a ten's kilometers in the N/NW direction. In-situ surface temperature observations collected from 14 to 17 March show SST cooling of ~ 3.5°C (29°C to 25.5°C) in 72 h - during these three days the animal remained quasi-stationary and only moved by a few kilometers. As the storm progressively moved south-eastwards, ST India began to slowly move to the NW, over the area previously affected by the tropical cyclone. Observations collected from 17 to 20 March show that the temperature surface layer in this area quickly returned to pre-storm conditions, to regain its initial temperature of 29°C on 19 March. As shown in Part II of this paper [33], surface and subsurface observations collected by STs in tropical cyclones can provide key data to evaluate coupled model forecasts in cyclonic conditions.

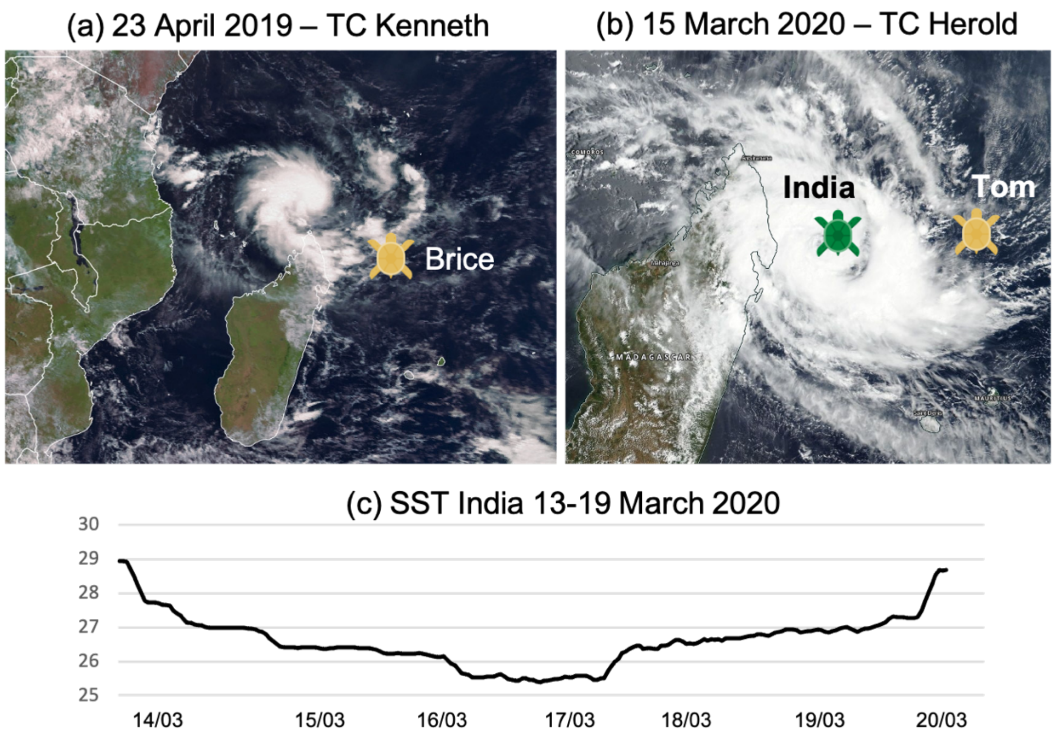

Figure 10: Satellite images of (a) TC KENNETH on 15 April 2019 and (b) TC HEROLD on 15 March 2020. Sea turtle symbols show the location of ST Brice during the cyclogenesis of TC KENNETH (left panel) and of STs India and Tom during the intensification phase of TC HEROLD (right panel). (c) Evolution of sea surface temperature (°C) in the vicinity of TC HEROLD as measured by ST India between 14 and 20 March 2020 within the area [51.93-52.62°E; 13.9/14.67°S].

3.1.4 Glider observations

On 22 January 2019 two SlocumG1 gliders operated by CNRS were deployed from Reunion Island for a period of 2 months. The two instruments were programmed to respectively follow a NE (glider GLNE) and a NW (glider GLNW) trajectory to reach the northernmost region of the Mascarene Archipelago, where a high probability of TC formation was suggested about 400-600 km north of Reunion Island (Fig. 11). The data acquisition strategy was set in order to complete a saw-tooth navigation pattern allowing the gliders to dive with an angle of 26° between 5 m and 980 m depth (resulting in an along-track resolution of about 4 km once the profile is normalized on the vertical).

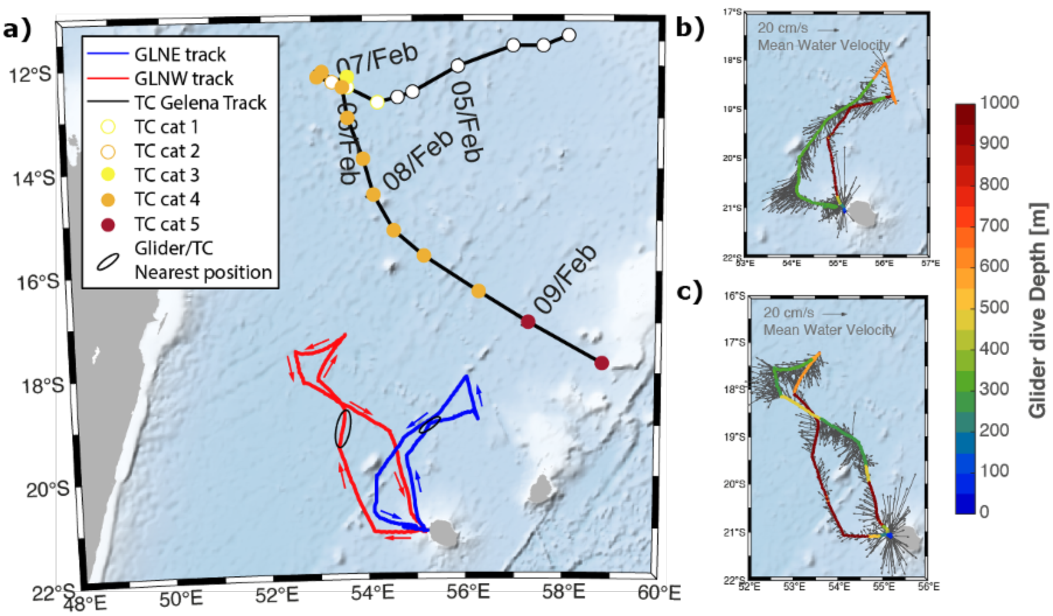

Figure 11: Trajectories of the two gliders deployed from Reunion Island between 22 January 2019 and 22 March 2019. (a) Trajectories of glider GLNE (blue) and GLNW (red), together with the trajectory and intensity (colored dots) of TC GELENA between 5-9 February. The position of the gliders during the TC period are indicated by black ellipses. Right panels show cast depth range and mean current velocities along the glider tracks estimated from glider drift for (b) GLNW and (c) GLNE. Table 1: Glider instrumentation, sampling rate (Hz), vertical resolution (m) and depth range (m) of collected data

The two gliders were programmed to sample the ocean during descending (downcast) and ascending (upcast) profiles. Observations were transmitted in real time by satellite telemetry after each upcast, when directives for modifying the sampling strategy and glider navigation (based on operational ocean model forecasts) were also received. Each glider was equipped with various physical and optical biogeochemical instruments for sampling the ocean temperature, salinity, oxygen, turbidity and chlorophyll-a concentration at different rates according to depth as shown in Table 1. All sensors were operational for glider GLNW while the oxygen and optical sensors were turned off on GLNE.

The primary objective of this experiment was to investigate kinetic energy exchanges between the ocean and the atmosphere in cyclonic conditions, with emphasis on the fraction of kinetic energy transmitted to the ocean. As shown by [102] who analyzed the vertical structure of the ocean in a tropical cyclone sampled during the CIRENE field phase [103], this kinetic energy is generated on the left side of the TC track in the southern hemisphere, and later consumed by strong vertical mixing resulting from surface water cooling [104]. Due to the presence of strong currents (> 0.25 m s^{-1}) along the glider trajectories, an important surface drift prevented the full application of the initially planned northward navigation strategy. The navigation parameters were then modified early in the mission to mitigate the battery consumption by reducing the depth range of the glider (as the oil pump that controls the glider buoyancy is the device that consumes the most energy). The gliders profiles were thus reduced to 500 m and 300 m depth (as shown by the colored tracks on Fig. 11b-c). Real-time data transmission was also turned-off at some point to reduce the time spent at the surface, when drifting was maximized. The slower than expected displacement speed of the gliders prevented them from intercepting the core of TC GELENA, which evolved in the area between 5 and 9 February 2019 (Fig. 11a). Thanks to real-time trajectory optimization, both systems were nevertheless able to approach relatively close to the storm, as shown by black ellipses displayed in Fig. 11a. The glider GLNE was for instance able to move to a distance of about 290 km from the TC center to collect ocean data in the direct vicinity of this storm.

Table 1: Glider instrumentation, sampling rate (Hz), vertical resolution (m) and depth range (m) of collected data

Parameter	**Instrument**	**Sampling**	**Resolution**	**Depth**
GLNE				
Temperature Salinity & Depth	CTD Seabird SBE-41cp	1/8	1.5	-5 to -980
Oxygen	Aanderaa Optode 5013	-	-	-
Fluorescence Turbidity	Wetlabs flbbcd	-	-	-
GLNE				
Temperature Salinity & Depth	CTD Seabird SBE-41cp	1/8	1.5	-5 to -980
Oxygen	Aanderaa Optode 4831	-	-	-
Fluorescence Turbidity	Wetlabs flbbcd	-	-	-

Vertical profiles of temperature, salinity and density collected by the two gliders between 0 and 150 m and 23 January - 17 February 2019 (along the 2 northward segments of the tracks) are shown in Figure 12, together with corresponding mean profiles for each parameter. The mixed layer depth (MLD), indicated by a black solid line, is estimated as the depth where the temperature differs by 0.2°C from a surface reference value of 10 dbar [105,106]. Due to the significant distance separating the two gliders from the TC core, and since the maximum kinetic energy generated in the upper ocean occurs on the left side of the TC track, no significant change in the surface temperature can be noticed during the pre-cyclonic, cyclonic and post-cyclonic phases (Fig 12a,d,g). A relatively constant temperature of 29°C is observed between the surface and 30 to 40m depth, but quickly decreases to reach 22°C at the depth of 150 m. Salinity measurements (Fig. 12b,e,h) indicate a freshening of the water within the top 100 m layer, starting around 6 February (-19.22°N) for the GLNW track, and from 28 January (-20.15°N) for the GLNE track. While part of this freshening can be explained by the rainfall generated by TC GELENA between 15°S and 5°N, another possible explanation is related to the advection of fresher water originating from the southern branch of the South Equatorial Current, which flows westward with a 20 Sv transport to feed the East Madagascar Current [107]. The velocity field computed from Mercator-Ocean's global reanalysis model PHY-001-030, which indicates the presence of strong westward currents between 28 January and 9 February (not shown), and the vertical extent of this fresh water lens both seem to support this hypothesis. Density measurements (Fig. 12c,f,i) do not seem to be impacted by this freshening and show a well-mixed layer within the top 40 m of the ocean and a well stratified layer underneath.

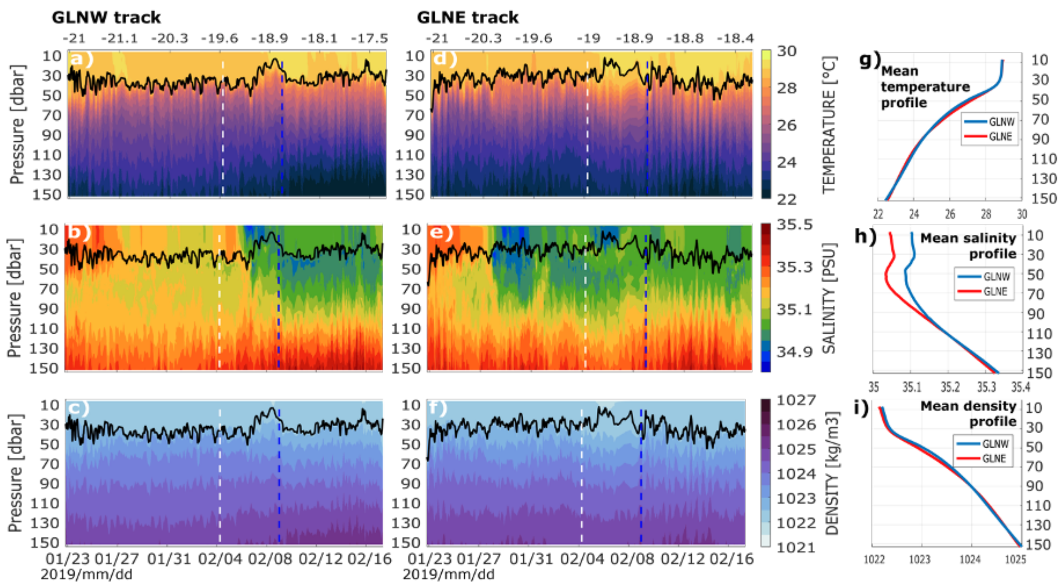

Figure 12: Time series of vertical temperature (top), salinity (middle) and density (bottom) profiles within the top 150m ocean layer from 23 January 2019 to 17 February 2019 for (a, b, c) GLNE and (d, e, f) GLNW tracks. Panels (g, h, i) show the associated mean vertical profiles over the same period. The vertical white dashed line in (a-f) indicates the date of formation of the Tropical Cyclone GELENA (4 February). The vertical blue dashed line shows the closest position of each glider to the TC core (around 9 February). The top axis indicates the latitudinal location of the profiles.

The mixed layer depth shows significant frequency variations in relation to the diurnal cycle, and also appears deeper along the GLNW track until 8 February. Since GLNW was always located southward of GLNE before this date, these observations suggest a sloping up of the MLD in the northward direction. As GLNW moves northward of GLNE after 8 February, the MLD measured by GLNE becomes deeper, thus reinforcing the hypothesis of a northward sloping up MLD. A significant rise of the MLD of up to 20 m (on 5 and 6 February for GLNE and GLNW, respectively) can also be observed almost immediately after the TC formation (4 February). The MLD then went back to its initial value between 9 February (for GLNW) and 12 February (for GLNE).

The Temperature-Salinity (TS) diagrams collected along the full glider tracks (23 January to 23 March 2019) are shown in Figure 13. The water masses sampled by the two instruments, known as the Indian Central Water, is formed and subducted in the Subtropical Convergence area of the southern gyre of the Indian Ocean [107-108]. The OML in this water mass was generally between 50 and 150 m depth, with temperature between 25 and 30°C and salinity in the range of 34.9-35.4 psu. Observations collected from the bottom of the OML to 1000 m show salinity values between 34.5 and 36 psu and temperatures decreasing from 25°C to 5°C.

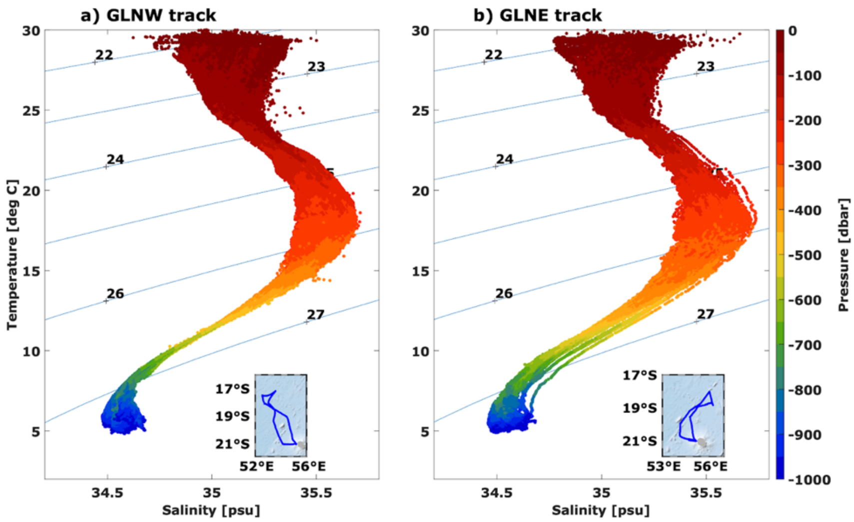

Figure 13: Temperature-Salinity (TS) diagram along (a) GLNW and (b) GLNE tracks from 23 January to 23 March 2019. Inserts show corresponding glider tracks.

3.2 Atmospheric observations

3.2.1 UAS observations

During RNC-CYC field phase, a UAS system called "BOREAL" was operated from Reunion Island to sample the lower part of the atmosphere (Fig. 14). The main objective of this experiment was to provide in-situ measurements of air-sea interactions in cyclonic and pre-cyclonic conditions to evaluate numerical models and microphysical parameterizations developed in the frame of the program.

The BOREAL UAS (Boréal SAS, Toulouse, France) is a fixed-wing aircraft with a 4.2 m wingspan using a thermal engine, with a maximum take-off weight of 25 kg (Fig. 14b). For this experiment, a 5 kg scientific payload has been developed to study air-sea interactions using an optical particle counter for measurements of aerosol number size distribution (0.3 < diameter < 3.0 µm; MetOne), a custom-designed multi-hole probe for measurements of turbulence and three-dimensional winds, a radar altimeter for wave height and sea state measurements, a broadband shortwave pyranometer for downwelling solar radiation (Licor), an infra-red temperature sensor to measure sea-surface temperature, as well as standard meteorological measurements (atmospheric pressure, temperature and relative humidity). A live video was also streamed up to 40 km from the ground-station to provide additional safety during low altitude segments when the UAS flow ~ 40 m above sea level (asl). The BOREAL UAS is autonomous, yet its flight plan can be adapted at any time to accommodate weather conditions or air traffic via a radio or a satellite link. A transponder mounted on its wing also allowed to integrate it in international airspace.

The BOREAL UAS flew over the Indian Ocean in two exclusive zones allocated by the French aviation authority to the southeast and northwest sides of Reunion Island (Fig. 14a). These areas were dedicated for scientific flights over the international waters up to 250 km from the ground station and with a ceiling at 1067 m above sea level. BOREAL UAS operations were conducted from the airfields of Cambaie (when flying towards the north of the island) and Bras Panon (when flying towards the south). In total, 12 scientific flights were carried out between February and March 2019, for a total of 53.7 hours of research flights and 5012 km of observations over the ocean. Three flights of more than 200 km from the ground station were carried out, the longest flight of which lasted 6 hours 18 minutes and covered 610 km. Examples of observations collected by the BOREAL UAS during this two-month operating period are presented below.

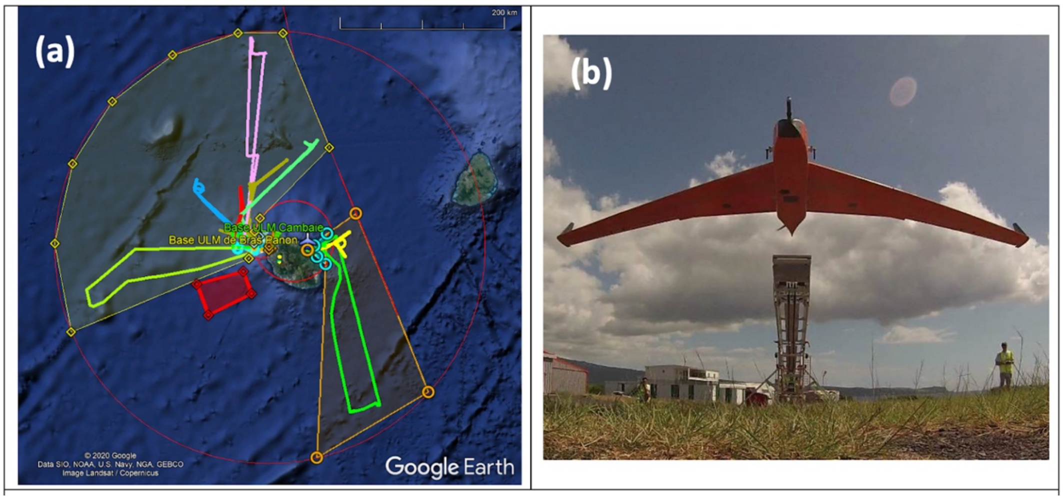

Figure 14: (a) The 12 BOREAL flights operated from Reunion Island during the RNR-CYC campaign in February and March 2019. The yellow and orange polygons represent the authorized flight zones to the northwest and southeast of Reunion Island. The outer red circle denotes an operating radius of 250 km around Reunion Island. (b) The BOREAL UAS leaving the catapult for a scientific mission from Cambaie, Reunion Island.

Figure 15 summarizes BOREAL UAS measurements of aerosol concentrations for particle diameters > 0.3 µm and > 1.0 µm within 200 m above the ocean surface, compared to horizontal wind speed (Fig. 15a) and wave height (Fig. 15b) for conditions encountered during the 2-month campaign. As expected, there is an increase in particle concentrations (diameter > 0.3 µm), which is often associated with primary marine aerosol (PMA) emissions, over the observed range of wind speed (2.2 to 13.5 m s^{-1}) and wave heights (2 to 3.7 m). However, the range of wind speeds and wave heights encountered in the vicinity of Reunion Island during RNR-CYC field campaign remained relatively small, in part because the paths of the TCs were never closer than a few hundred kilometers to the ground station during the observed period.

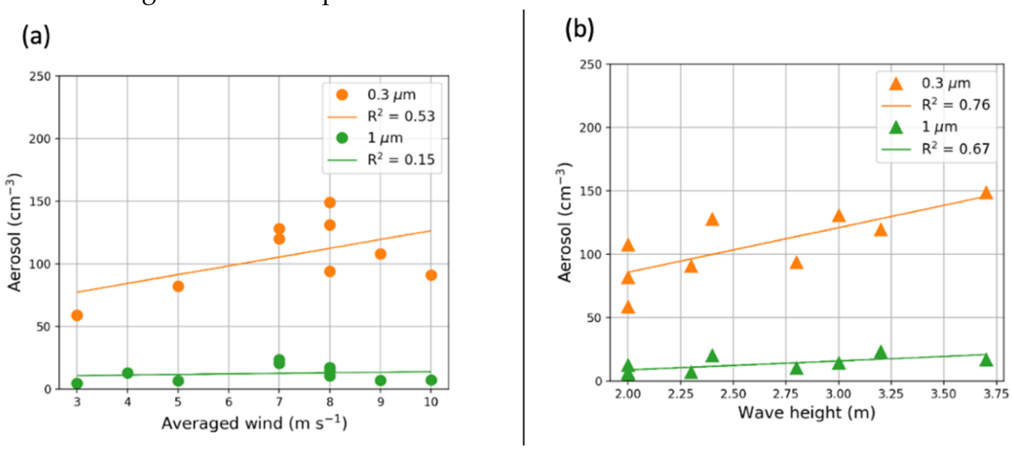

Figure 15: Aerosol concentrations (diameter > 0.3 µm and > 1.0 µm) measured during the BOREAL flights as a function of (a) the averaged horizontal wind in the marine boundary layer and (b) the measured wave height.

Although strong cyclonic conditions were not encountered in the vicinity of Reunion Island during the 2019-2020 TC season, several BOREAL UAS flights were nevertheless impacted by the presence of TC JOANINHA, which developed in the eastern part of the Mascarene Archipelago in March 2019 (Fig. 16a). The signature of this storm could be seen up to several hundred kilometers away in observations of ocean waves, atmospheric turbulence structures and enhanced PMA emissions – The emissions, which occur over a much larger domain than the cyclonic system, have been shown to modify the TC's track and intensity [11].

As TC JOANINHA moved to the east of Mauritius, the BOREAL UAS flew on the west of Reunion Island to sample the TC's perimeter (see flight track in Fig. 16a and wave crests, swells and clouds generated by the cyclone recorded by the on-board camera in Fig. 16b). In-situ measurements were used, in particular, to assess parameterizations of air-sea interactions simulated with the OWA coupled system developed in RNR-CYC (see [33] for details about this system). Results presented hereafter are derived from a single coupled OWA simulation based on the models Coastal and Regional Ocean Community (CROCO[5]), WW3 [94,95] and Meso-NH[6], that was developed specifically for comparisons with the BOREAL UAS.

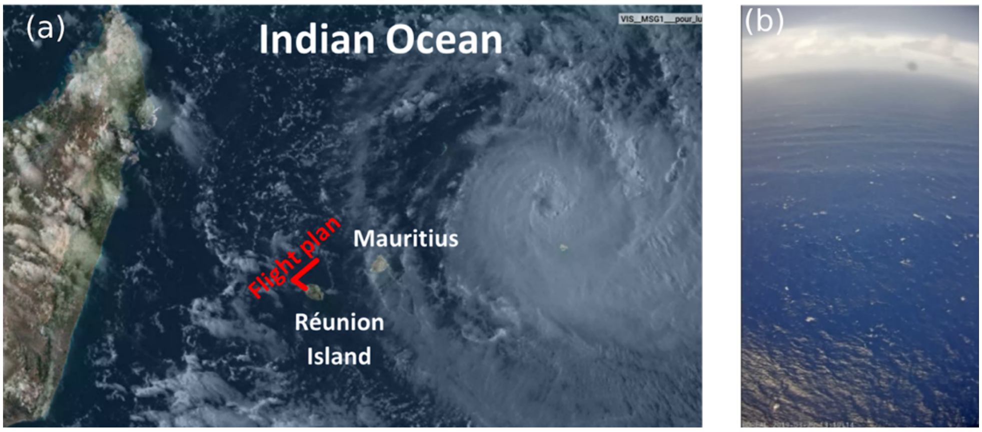

Figure 16: (a) Satellite image of TC Joaninha on 25 March 2019 in the vicinity of Mauritius and Reunion Island. (b) picture from the BOREAL on-board camera showing the ocean sea-state and the Joaninha TC on the horizon.

Figure 17 presents a vertical profile of aerosol particles conducted during the 25 March flight from near the ocean surface (< 50 m asl) to above the marine boundary layer (~ 1000 m asl). Observed aerosol concentrations (diameter > 0.3 μm) are found relatively constant throughout the marine boundary layer (up to ~ 800 m asl) and decrease above the inversion. A surface layer with enhanced emissions, similar to the profiles observed at the surf zone in the frame of project Miriad [109], is also observed at the lowest part of the vertical profile (~ 50 m asl). This surface layer, which was not captured in the model simulation (Fig. 17), has not been well-documented so far and has important implications for the transport of aerosol into the well-mixed boundary layer. In addition, the simulations tend

[5] http://www.croco-ocean.org

[6] http://mesonh.aero.obs-mip.fr/

to overestimate the aerosol emissions near the ocean surface (i.e., ~ factor of two enhancement in aerosol concentrations) and show a pronounced vertical gradient throughout the marine boundary layer with an underestimate of aerosol concentrations in the free troposphere.

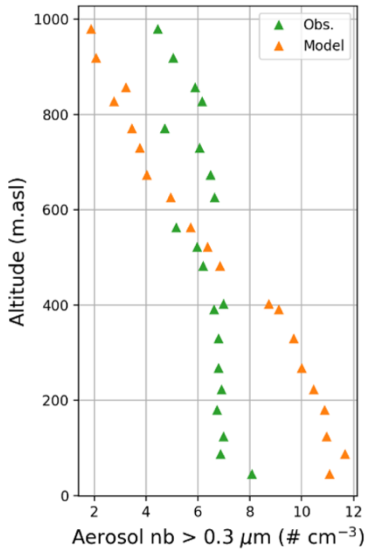

Figure 17: BOREAL profile of aerosol number for particles larger than 0.3 μm obtained with the onboard Optical Particle Counter (green) and simulated with the OWA model (orange).

A few days later, a southern swell event occurred when winds shifted to the north-east direction as TC JOANINHA continued its eastward progression through the Indian Ocean. Flight operations were moved to Bras Panon and the BOREAL UAS flew along a southern curtain for more than 200 km to the east of Reunion Island on 29 March 2019 from 6:33 to 12:04 UTC (Fig. 18a). The platform followed a purposing flight plan with ascents from 100 to 1000 m asl followed by straight-level legs at 400 and 100 m asl for at least 10 km each. Mean and significant wave height observations collected during this flight by onboard radar altimeter show that wave height increased by about a meter (from ~ 2.5 to 3.5 m) between locations A and D (Fig. 18b).

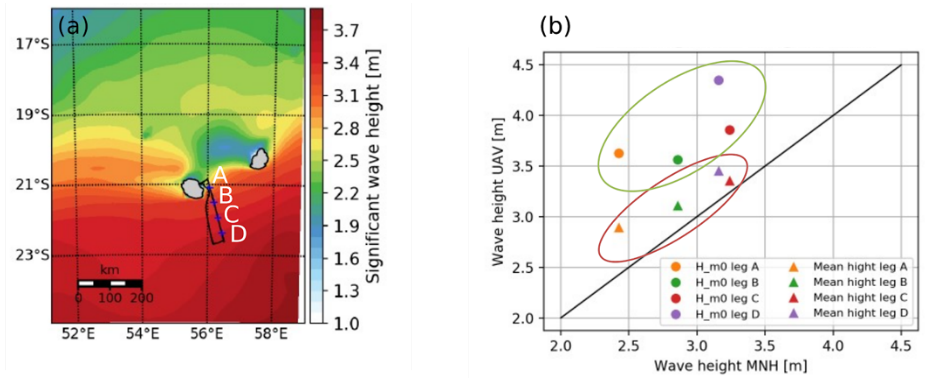

Figure 18: (a) WWW3 simulation of significant wave height on 29 March 2019 with the BOREAL UAS flight overlaid on the image (black line). The blue crosses correspond to A, B, C and D legs of the flight at 100 m asl.; (b) Significant wave height (H_m0) and mean wave height from the BOREAL UAS observations compared to wave height simulated by WWW3.

A similar increase of wave height is also obtained in the simulations of this case study made with the *WaveWatch3* model (Fig. 18a). The associated modelled (Fig. 19a) and observed (Fig. 19b) spectral density functions provide insight on the composition of the southern swell and show two peaks for both observations and simulations. Azimuth plots from *WW3* based on the wave elevation spectrum (Fig. 19c) indicate that these peaks correspond to distinct components of the southern swell; the first component is generated by the northerly winds (red arrow in Fig. 19c) and the second component is generated by TC JOANINHA to the east (black arrow in Fig. 19c). In spite of the observed increase in wave height (and relatively constant wind field) a horizontal gradient in the aerosol concentration and size distribution at 100 m asl was not observed during this swell event. These results were predictable as the 1 m increase in wave height is relatively small and not expected to generate a significant difference in PMA emissions.

Due to the low number of TC passing in the immediate vicinity of Reunion Island during the TC season 2018-2019, the range of wind speeds and ocean wave conditions were not as large as expected to fully assess parameterizations for PMA emissions. Nevertheless, the datasets collected during this campaign have clearly demonstrated the scientific potential of the BOREAL UAS, and of its associated payload, to collect key observations in remote oceanic areas and in the vicinity to tropical cyclones.

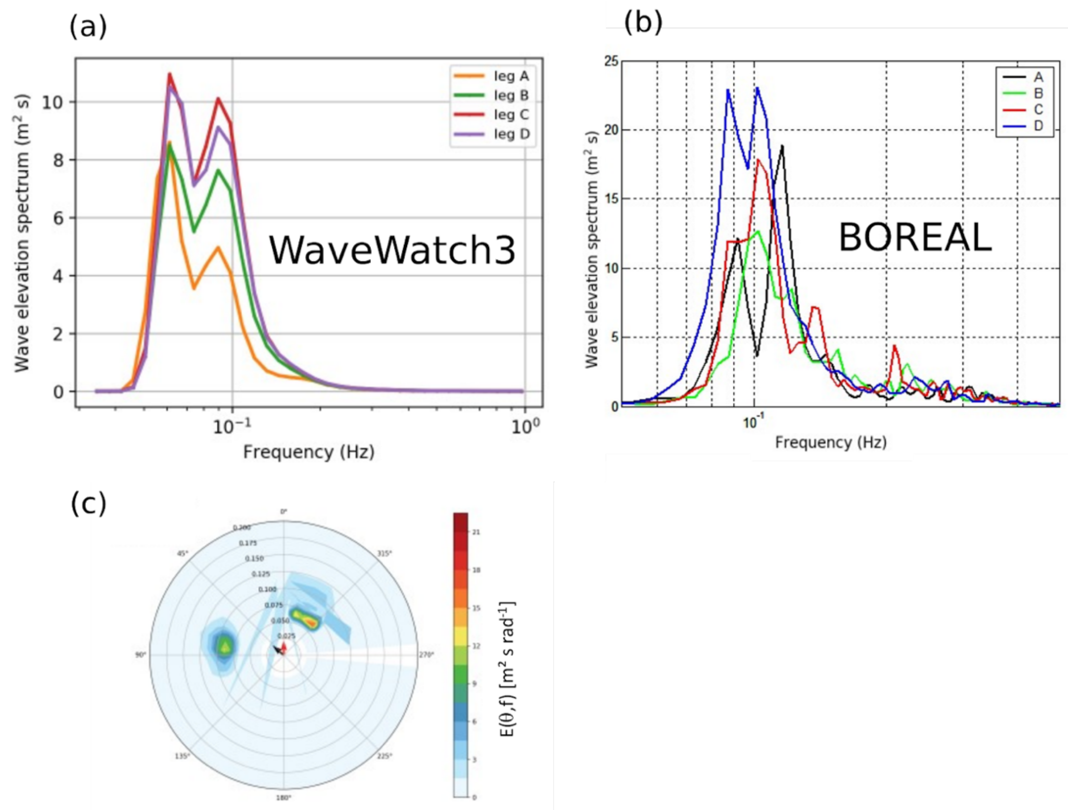

Figure 19: (a) Spectral density function of wave height simulated with WWW3 for legs A, B, C, and D. (b) Spectral density function of wave height from BOREAL UAS observations for legs A, B, C, and D. (c) Corresponding azimuth plots to wave elevation spectrum. The arrows represent the wind direction and the scatter color plots are the wave crests

3.2.3 GNSS observations

A well-known indirect atmospheric application of GNSS measurement consists in measuring the integrated water vapor (IWV) content from the delay induced by water vapor during the crossing of the earth's atmosphere by the GNSS signal [110]. Due to the fundamental role of water vapor in climate and weather dynamics, tropospheric GNSS measurements have rapidly become one of the main tools used by climatologists to monitor the evolution of the water vapor field at all spatio-temporal scales, but also to improve NWP model forecasts (see [111] for a recent review of current GNSS weather applications). The creation of the International GNSS Service (IGS) network in 1994 [112], which now includes more than 500 stations worldwide, has also enabled GNSS-derived measurements collected in all parts of the world to be widely disseminated to the scientific community. With only 8 operational stations available prior to RNR-CYC (Fig. 20), the density of public GNSS stations in the SWIO was, however, the lowest of all TC basins.

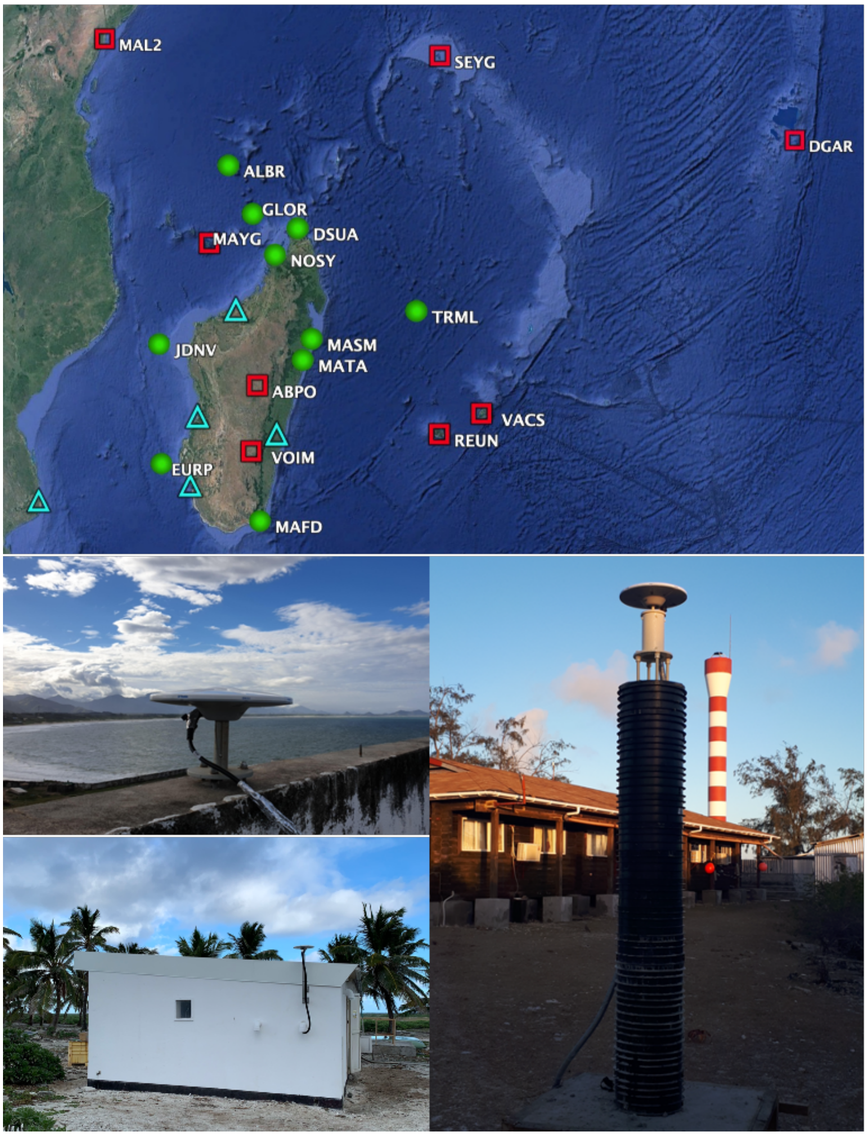

Figure 20: Map of public GNSS stations available in the SWIO as of March 2021 (top). Red squares show current IGS stations, green dots show GNSS stations installed during RNR-CYC and blue triangles show stations to be installed in 2021 in the frame of the newly project ESPOIRS (see Section 4). Pictures show GNSS stations installed in Fort-Dauphin (MAFD, upper left), Tromelin (TRML, lower left) and Aldabra (ALBR, lower right).

During RNR-CYC, 10 new permanent stations have been deployed including one in the Seychelles (Aldabra), four in Eparses Islands (3 RNR-CYC stations at Juan de Nova, Tromelin and Europa and 1 shared station installed by OPGP in Glorieuses) and five in Madagascar (Diego-Suarez, Toamasina, Sainte-Marie, Nosy Be and Fort-Dauphin), with the goals to increase the density of the GNSS network in the SWIO and to provide additional near real-time IWV measurements at various locations in the basin (Fig. 20). Although these stations have not yet been included into the IGS network (pending), most collected GNSS observations are transmitted at hourly time step to IGN's data center, which already allows for routine real-time GNSS calculations and wide dissemination of derived meteorological and geophysical products through IGN's permanent GNSS network (RGP)[7].

These new stations have already been shown to represent a fantastic asset for monitoring the spatio-temporal evolution of the water vapor field at local and regional scales [34, 35] as well as to evaluate NWP forecasts [34]. A further example is shown in Figure 21, which presents differences between GNSS-derived IWV observations and IWV contents analyzed daily at 00, 06, 12, and 18 UTC with the operational, 2.5 horizontal resolution, NWP system AROME-IO [42] at Aldabra (ALBR, The Seychelles), Antananarivo (ABPO, Madagascar), Reunion Island (RUN, France) and Sainte-Marie (MASM, Madagascar) during year 2019. In order to evaluate the performance of the model at various time scales, 30-day (red), 10-day (yellow) and 3-day (black) moving averages were applied to both model and GNSS data. GNSS observations were processed following the approach proposed by [35].

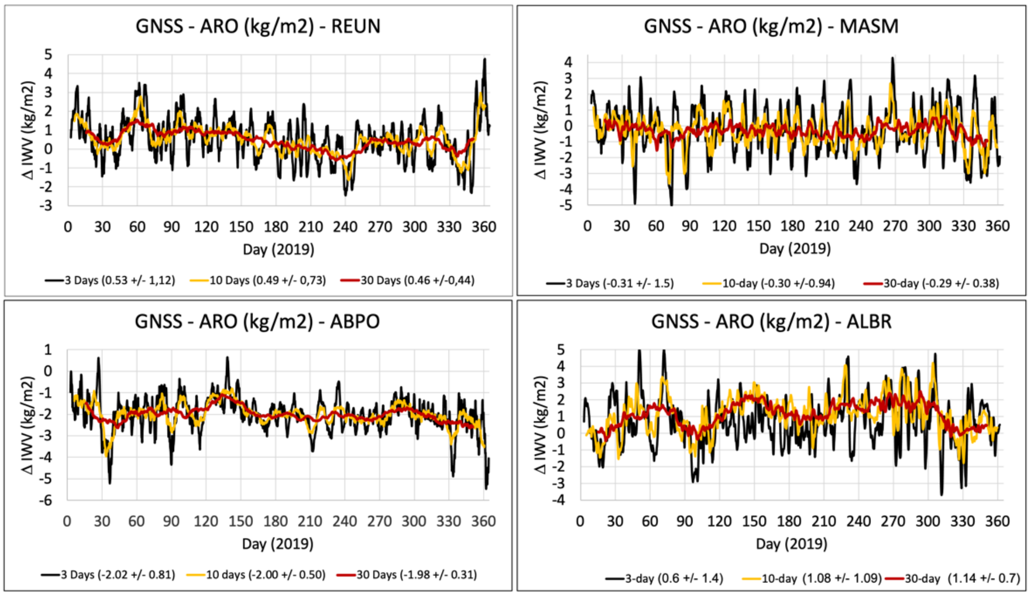

Figure 21: Time series of the differences between IWV contents observed by GNSS and analyzed by the model AROME-IO at Reunion Island (REUN, upper left), Sainte-Marie (MASM, upper right), Antananarivo (ABPO, lower left) and Aldabra (ALBR, lower right) throughout year 2019. 30-day (red), 10-day (orange) and 3-day (black) moving averages are applied to IWV data to evaluate the impact of short and mid-term moisture variations on the model performance.

[7] ftp://rgpdata.ign.fr/pub/gnssmayotte

Whatever the time scale, the bias error remains relatively constant at Sainte Marie (MASM, ~ - 0.3 kg m^{-2}), Reunion (REUN, ~ 0.5 kg m^{-2}) and Antananarivo (ABPO, ~ -2 kg m^{-2}), but shows more variations in Aldabra (ALBR, between 0.6 and 1.14 kg m^{-2}). The differences between the model and the observations do not show a clear seasonal dependency except at Aldabra where maximum errors are observed in the middle of the winter, spring and fall seasons. In the case of this atoll, consisting of land strips of 1 to 3 km width encircling a lagoon of nearly 30 km x 15 km, the land is considered as submerged by the model, which does not allow to take into account both the effect of vegetation and of the diurnal cycle on the atmospheric moisture content (atmospheric moisture variation thus mostly depend on the variation of the temperature of the ocean). Interestingly, the sign of the bias error is location dependent, suggesting that the model is not affected by systematic errors. The associated standard deviation errors also tend to decrease with the length of the smoothing period, which minimizes the impact of short-term variations. At short time scales (3-day), one can also notice that the strongest discrepancies mostly occur during the TC (wet) season (days 1-120 and 330-365), in relationship with the passage of tropical cyclones in the vicinity of the GNSS ground-based stations.

As already pointed out by [34], who investigated the seasonal variations of AROME-analyzed IWV errors at Diego-Suarez (DSUA), model-observation differences seem exacerbated for stations located in the vicinity of complex orography. If one except the particular case of Aldabra, the same behavior can be noticed here for the high-altitude stations of Reunion (600 m amsl, REUN) and Antananarivo (2000 m amsl, ABPO), which show higher errors than for the flat island of Sainte-Marie (MASM). These errors might be related to the difficulties of the model to properly capture the modifications of air masses caused by the orography (lifting and subsiding motions) at the local scale due to an insufficient resolution of its topography. A possible way to correct for such errors could be to assimilate GNSS observations (zenithal delays) into the model. While the operational version of the AROME-IO NWP system does not allow for data assimilation, its research configuration includes a 3D-Var scheme that can be used to perform assimilation experiments [34]. Some studies are currently ongoing to determine whereas the assimilation of GNSS observations can help reduce the model moisture bias.

3.3 Spaceborne observations

Visible and infrared satellite observations have long been the main source of knowledge for estimating some of the parameters (e.g., radius of maximum wind, various wind radii) characterizing the structure of tropical cyclones - these parameters are, in particular, inputs of the Dvorak method [113], used by TC forecast centers to produce best track data and issue TC advisory and forecasts. Since the launch of the first Earth observation satellite in the early 1970s, the quality of ocean surface wind estimates in the vicinity of TCs have been constantly improved. This includes for instance the deployment of wind scatterometers (e.g., [114,115]) as well as of multifrequency radiometers (e.g., [116,117]) that both allow for a direct, and more precise, estimate of surface winds under TCs. More recently, a new generation of microwave radiometers has also been put into operations by ESA and the National Aeronautics and Space Administration (NASA) in the frame of the Soil Moisture and Ocean Salinity (SMOS) and Soil Moisture Active Passive (SMAP) space missions, respectively. Thanks to their large coverage and revisit time, these new sensors, which allow for high-resolution (~ 40 km) surface wind speed sampling in all weather conditions, can provide a unique description of the TC structure during its whole lifetime [118] and have thus become a key source of information for TC forecasting centers.

In addition to these more or less conventional sensors, a new approach, based on the use of spaceborne synthetic aperture radars (SAR), is also being increasingly used to probe and quantify sea surface properties under extreme wind conditions. Designed in the mid-nineties, SAR systems were initially used for land application [119], especially for monitoring earth deformation rates ranging from a few mm per year (e.g., glaciers) up to 1 m per h (e.g., earthquakes and landslides). SAR potential for marine applications is known since the launch of the first SAR [120], but has significantly emerged with the launch of Canadian Space Agency (CSA)'s RADARSAT-1 (1995) and ESA's Envisat (2002) satellites. Thanks to their unique capability to gather very high-resolution (up to a few meters) surface wind and roughness data in swaths of several hundred kilometers, spaceborne SAR constitute key observing systems for monitoring, forecasting and investigating the properties and evolution of TC (e.g., [120,121]).

The deployment of a new generation of SAR systems equipped with polarization diversity onboard CSA's RADARSAT-2 (RS2, 2007) and ESA's Sentinel-1 (S1, 2014) satellites has allowed to further improve the capabilities of these instruments to accurately map the variations of ocean surface winds in TC eyes and eyewalls [122,123]. Acquisitions made by ESA's satellites have, however, never been used to probe tropical cyclones until the implementation of the Satellite Hurricane Observations Campaign (SHOC, 2016-2017), in the Pacific and Atlantic basins. The intercomparison of aircraft reconnaissance wind data against S1 SAR measurements collected in CAT-5 hurricane IRMA (2017) during this experiment has definitely demonstrated the capability of these instruments to thoroughly describe TC ocean boundary layer structures at high spatial resolution [124].

The extension of the SHOC program to the SWIO basin (referred to as SHOC-V2) was initiated in 2017, under the frame of RNR-CYC. Because SAR missions cannot continuously acquire wide swath data in high-resolution modes, a dedicated acquisition procedure was set up to collect data without impacting the operational duty cycle of the satellites. Acquisition requests were passed along to both MDA (MacDonald Dettwiler and Associates, the private company that owns the satellite RS2) and ESA S1 mission planner portals on a 24-to-48-h notice, based on satellite orbit and 5-day track forecasts provided by RSMC La Réunion. In order to reduce the workload of participating space agencies, which contributed to this experimental program on a voluntary basis, acquisition requests were also generally limited to storms presenting a threat to SWIO populations.

Between 2017 and 2021 about 150 SAR images were acquired by S1A, S1B and RS2 satellites[8], allowing to sample 20 tropical storms and cyclones over four TC seasons. Among these acquisitions, nearly 40% were directly obtained within the eye or the eyewall of the systems (Table 2, "hits"). SAR images were collected throughout the SWIO basin (Fig. 22) at various storm evolution stages (cyclogenesis, intensification, dissipation). Collected wind data were used for nowcasting and best-track data reanalysis purposes at RSMC La Réunion, model verification [33] and assimilation in NWP systems [125].

Table 2: Number of RS2 and S1 SAR acquisitions within the eyewall / eye (hits) of tropical storms (TS) and tropical cyclones (TC, ITC) that developed in the SWIO between February 2017 and 2021. * Acquisitions performed from 2021 on were made in the frame of the CYMS program (see Section 4).

Storm Name	Date	Hits	Storm Name	Date	Hits
Dineo (TC)	02/2017	2	Idaï (ITC)	03/2019	3
Enawo (ITC)	03/2017	1	Joaninha (ITC)	03/2019	7
Ava (TC)	01/2018	3	Kenneth (ITC)	04/2019	1
Berguitta (ITC)	01/2018	4	Lorna (TC)	04/2019	4
Cebile (ITC)	01/2018	8	Belna (TC)	12/2019	5
Dumazile (ITC)	03/2018	5	Calvinia (TC)	12/2019	1
Eliakim (TS)	03/2018	1	Diane (TS)	01/2020	1
Alcide (ITC)	11/2018	1	Francisco (TS)	02/2020	1
Kenanga (ITC)	12/2018	2	Herold (ITC)	03/2020	1
Gelena (ITC)	02/2019	4	*Chalane (TS)	12/2021	3
Haleh (ITC)	03/2019	6	*Eloise (TC)	01/2021	2

Examples of SAR-derived wind acquisitions obtained through the application of the retrieval algorithm proposed by [123] are presented hereafter. The first example is taken within TC JOANINHA, which developed in the northeastern part of the Mascarene Archipelago, and reached its LMI in the vicinity of Rodrigues Island on 26 March 2019 with 10-min maximum sustained winds of nearly 60 m s^{-1} (Fig. 23a). The core structure of this system was observed seven times by the SAR systems deployed onboard satellites S1A/S1B and RS2 (Table 2) at various stages of its life cycle. Of particular interest is the image taken

[8] Raw S1 data available at https://scihub.copernicus.eu/.

on 28 March 2019 at 00:52 UTC by RS2 (Fig 23b), when the system started to experience an eyewall replacement cycle (ERC).

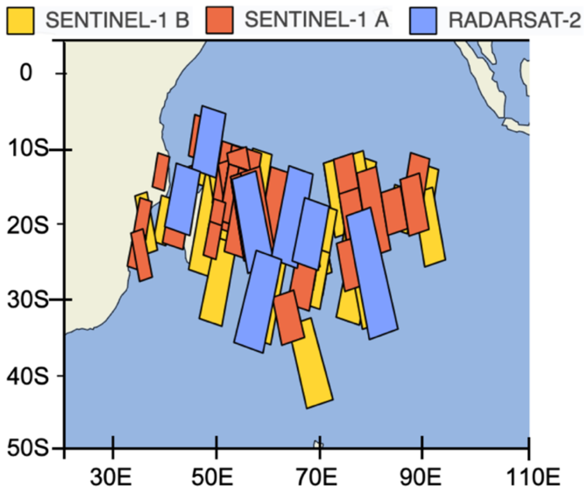

Figure 22: Location of Sentinel-1 (A&B) and RADARSAT-2 swaths listed in Table 2.

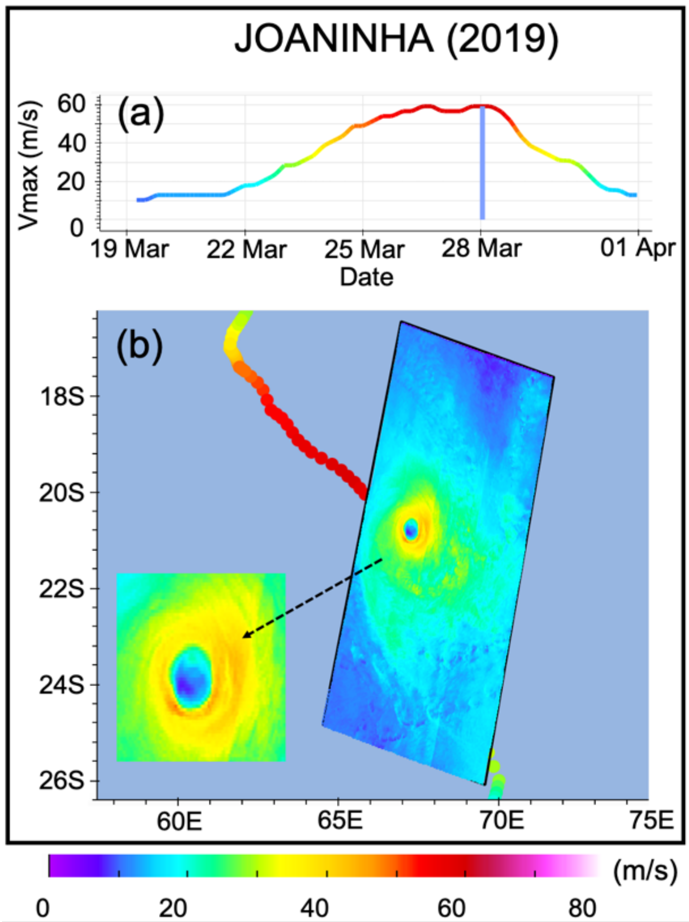

Figure 23: Intensity of TC JOANINHA (color scale at bottom). (a) Wind speed evolution with respect to time as given by ATCF and (b) SAR wind retrieval (RS2) on 28 March 2020 at 00:52 UTC.

ERCs, which often occur when a TC reaches an intensity of 50 m s^{-1}, have long been recognized as one of the main mechanisms for intense TC to intensify further (e.g., [126, 127]). During an ERC, outer rainbands strengthen and organize themselves into a ring of thunderstorms that progressively encircles the TC eyewall. The formation of this outer ring, usually referred to as the outer eyewall, eventually cuts off the alimentation in moisture and angular momentum that maintain the convection around the eye, causing a weakening of the system and the eventual dissipation of the inner eyewall. The former ring is then replaced by the outer one, which gradually contracts and intensifies, often resulting in a more intense TC than prior to the ERC. The analysis of the SAR-derived surface wind field shown in Figure 23b clearly indicates the presence of two concentric areas of maximum wind located both around the eye and in the east-to-southeastern quadrant of the system core. The inner structure (maximum wind speed of ~50.2 m s^{-1}) corresponds to the eyewall of the storm and the outer one (maximum wind speed of ~45 m s^{-1}) to the cyclonic rainbands progressively wrapping around the eyewall that will eventually replace the inner wall. The completion of an ERC is often followed by a re-intensification of the system. However, in the present case such re-intensification did not occur as TC JOANINHA rapidly encountered a strongly sheared environment that caused its dissipation a couple of days later.

The second example is taken from TC IDAÏ (Fig. 24). As mentioned previously, this storm is considered as the worst natural disaster that has ever affected Mozambique (as well as surrounding countries of Zimbabwe and Malawi), and the deadliest storm ever recorded in the SWIO. This unique TC initiated as a tropical depression along the northern coast of Mozambique on 3 March 2019 (Fig. 24a) and moved inland in the northwestern part of the country for a few days, with peak winds in the order of 10-15 m s^{-1}. On 7 March, it made a half-turn near the Mozambique-Malawi border to move back towards the ocean. After entering the Mozambique Channel, on 9 March, the storm immediately experienced a rapid intensification to reach intense TC intensity (10 min maximum sustained wind > 46 m s^{-1}), with winds gusts estimated to up to 70 m s^{-1} on 11 March. IDAÏ then reversed its track back for the second time in the immediate vicinity of the Eparses island of Juan de Nova (located approximately 150 km off the west coast of Madagascar) and began its southwestward propagation towards Mozambique. Shortly after this half turn, it entered into a slight weakening trend following the beginning of its ERC. Right after its completion, IDAÏ immediately re-intensified to reach its LMI on 14 March, with a minimum central pressure of 940 hPa and (estimated) 10-min maximum sustained winds of ~55 m s^{-1}. The storm then gradually weakened while progressing towards the coast of Mozambique, where it made landfall at Beira on 15 March at the stage of TC.

Numerous acquisitions were made in this system by S1 satellites, including three images collected directly in the core of storm (Fig. 24b). Two of these hits were made over the ocean by S1A, at the stage of intense TC (11 March at 2:43 UTC and 14 March at 3:08 UTC), while a third one was made near landfall by S1B on 14 March at 16:00 UTC (as 90% of this swath occurred over land, this third acquisition is however not exploitable). Because SAR wind data shown in Figure 24 are the only high-resolution wind observations collected during the oceanic phase of this system - WMO's JDN weather station broke down a week before the passage of the storm over the island and the weather station deployed at Beira in the frame of RNR-CYC was lost during landfall - these observations represent an invaluable asset for accurately assessing numerical model simulations of this storm [33].

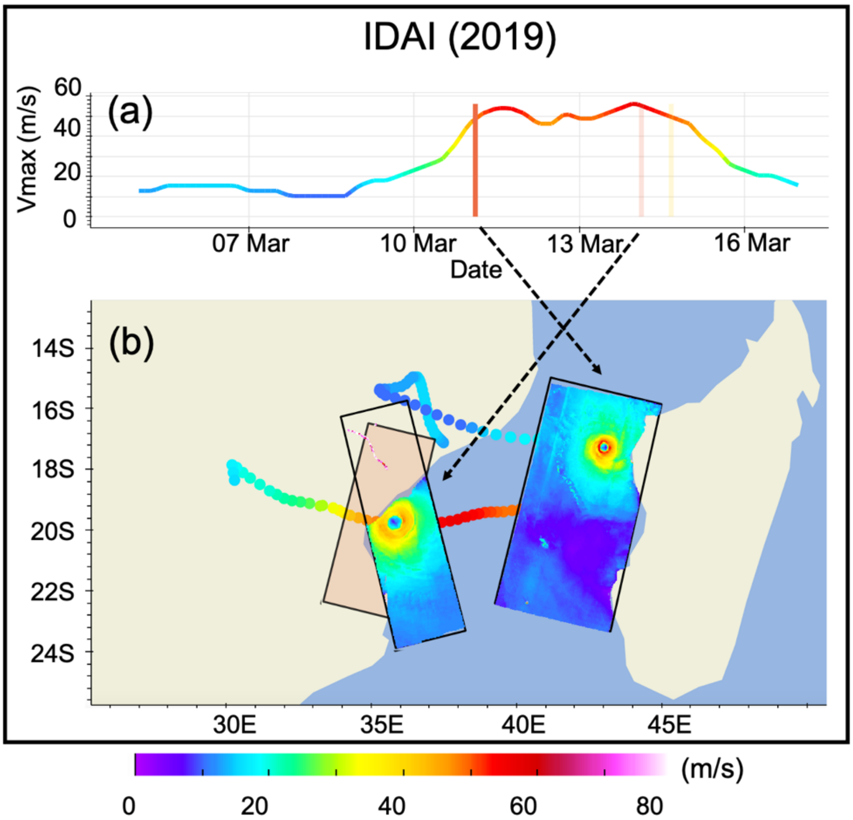

Figure 24: As in Fig. 23, but for TC IDAÏ and SAR images collected in by S1A on 11 (2:43 UTC) and 14 (03:08 UTC) March 2019.

These observations, together with SAR data collected in other systems, can also meaningfully complement best-track (BT) data produced by RSMC La Réunion. According to BT data, TC IDAÏ reached its LMI on 14 March 2019 at 00 UTC with a wind speed of nearly 55 m s^{-1}. This value is in good agreement with the maximum intensity measured by S1B a few hours later (~52 m s^{-1}). SAR data, however, suggest that these high intensity values were only observed in the eastern quadrant of the storm's core, but that the average wind speed throughout the eyewall was significantly less intense and mostly comprised between 42 and 45 m s^{-1}. On 11 March, the agreement between best-track and SAR-derived wind data is less good, with maximum wind speed in the order of 50 m s^{-1} for the BT and 60 m s^{-1} for SAR observations. According to SAR observations, the strongest wind speed values were also more or less uniformly distributed throughout the eyewall. The comparison of the two SAR images hence suggests that the destructive potential, and overall global intensity of the system, was probably much greater on 11 March, despite a 10% lower maximum wind speed (50 m s^{-1} vs. 55 m s^{-1}) in BT data.

4. Conclusions and Perspectives

ReNovRisk-Cyclone (RNR-CYC) is an ambitious international research program aimed at developing regional cooperation in the SWIO with emphasis on the observation and modeling of tropical cyclones at both current and future time horizons. The observing component of RNR-CYC, presented in details in this paper, has allowed collecting numbers of innovative oceanic (gliders, sea-turtle borne and seismometer-derived data) and atmospheric (UAS and SAR-derived wind data) measurements, together with more conventional observations (GNSS-derived IWV, atmospheric radiosoundings, ADCP and wave gauge swell measurements) to investigate tropical cyclones and their environment from the local to the basin scale. Its mesoscale modelling and climate components, presented in more details in the companion paper [33], also allowed for the development of innovative modelling systems, while its outreach component significantly increased regional collaboration between SWIO countries affected by TC hazards.

The promising results obtained during the 3 ½ y observation component of RNR-CYC have led to the development of several new projects aimed at further reinforcing observations capabilities in the SWIO beyond the end of this program (July 2021). Among the new research programs directly or indirectly arising from RNR-CYC, one can cite projects STORM-IO (Sea Turtle for Ocean Research and Monitoring in the Indian Ocean), ESPOIRS (Etude des systèmes précipitants de l'océan Indien par radar et satellites - Studies of Indian Ocean precipitation systems by radars and satellites) and MAP-IO (Marion dufresne Atmospheric Program - Indian Ocean). These new projects, also funded by the EU and the Regional Council of Reunion Island, will allow further strengthening oceanographic and atmospheric measurements in the Indian Ocean through the continuation, or the reinforcement, of observation programs initiated in RNR-CYC.

STORM-IO (starting May 2021) will allow extending ST-borne measurements conducted from Reunion Island to the whole Indian Ocean (Fig. 25), in collaboration with the Terres Australes et Antarctiques Françaises (TAAF) administration in Eparses Islands of Juan de Nova and Tromelin, Kelonia (Reunion Island) and five marine reservations in Comoros (Moheli), Madagascar (Nosy Tanikely), Seychelles (Aldabra), Mozambique (Ponto di Ouro) and South Africa (iSimanlisao). This transdisciplinary project, constructed in close cooperation with ST specialists and oceanographers, will allow extending the research work initiated in RNR-CYC to: i) investigate the thermodynamics and spatio-temporal variability of the IO at high space-time resolution, and ii) improve knowledge of the ecology of the five species of sea turtles living in the Indian Ocean. A particular emphasis will be put on the observation of mesoscale eddies and coastal currents that develop in the Mozambique Channel (to assess their impact on water mass distribution, transport and mixing, as well as their overall role in the dynamics of the Greater Agulhas current system) as well as ST-borne data assimilation in global and limited-area configurations of the ocean model NEMO [129].

ESPOIRS (started in December 2020) will carry on with the densification of the GNSS water vapor observation network initiated in the framework of RNR-CYC through the deployment of 5 additional stations in Madagascar and Mozambique (Fig. 20). Existing, or soon to be deployed, GNSS stations will also be upgraded with co-located oceanographic sensors to monitor the sea level on a regional scale. Thus, one of the objectives of ESPOIRS is to provide long-term measurement to the Global Sea Level Observing System (GLOSS) network that monitors sea level rise on a global scale[9]. ESPOIRS also includes an ambitious local component aimed at collecting wind and precipitation measurements in tropical cyclones by the mean of a transportable polarimetric weather radar to be deployed alternately in Reunion Island (2021), Madagascar (Tamatave or Diego Suarez, 2022) and the Seychelles (Mahe, 2023). This radar component will allow to further investigate the impact of orography on the structure, intensification and track of tropical cyclones (and outer cyclonic rainbands in the Seychelles) passing in the vicinity of islands characterized by a complex terrain [130] as well as to reinforce regional cooperation in atmospheric remote sensing.

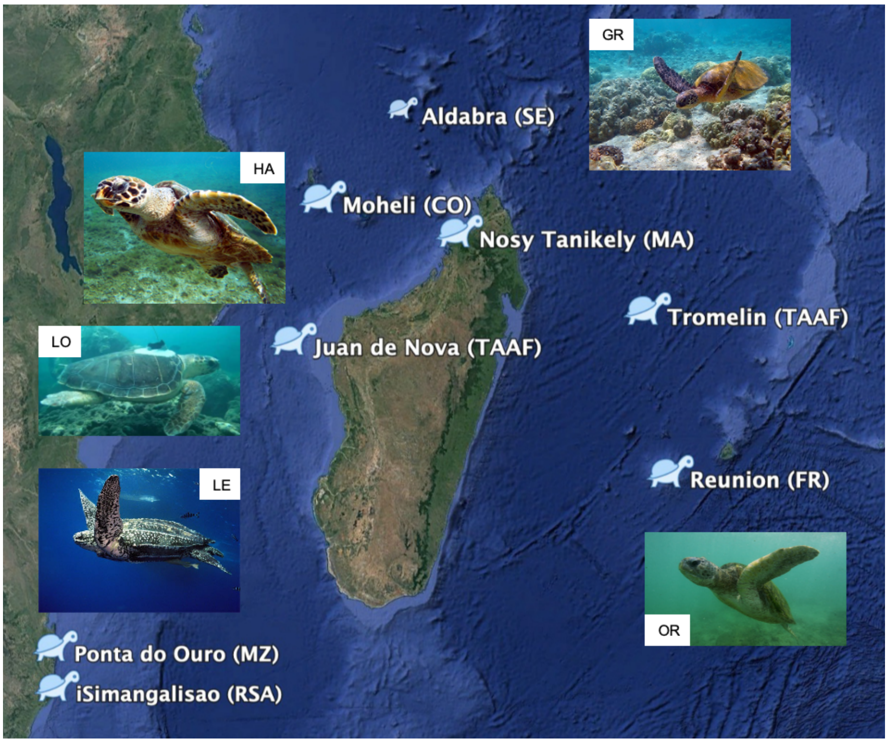

Figure 25: Release locations and type of sea turtles (OR: Olive Ridley, GR: Green, LE: Leatherback, LO: Loggerhead, HA: Hawksbill) to be equipped in the frame of the STORM-IO project

The MAP-IO program aims to deploy an atmospheric and marine biology observatory in the Indian and Southern Oceans onboard the French vessel Marion Dufresne (Fig. 26), operated by the TAAF administration (for its logistical needs in the Eparses Island and French Austral Territories) and IFREMER (for scientific campaigns in the IO). With the deployment of nearly 20 new sensors onboard this RV (e.g., cytometer, titrator, thermosalinograph, cytometer, titrator, NOx, CO, CO2, O3 and CH4 analyzers, GNSS, UV radiometer, CCN, photometer, weather station), MAP-IO will permit the collection of long term, permanent, observations at the ocean-atmosphere interface and within the atmospheric column in this region particularly sensitive to the impact of climate change (note that all observations will be transmitted in near real time through the RV onboard satellite communication system). The data collected in the Southern Ocean for sea and wind states close to those encountered in tropical cyclones will also allow to develop and evaluate

[9] https://www.gloss-sealevel.org/

more precisely the parameterizations of AO exchanges (turbulent fluxes, aerosol and sea-spray emissions) in extreme conditions.

Figure 26: Picture of the RV Marion Dufresne anchored at Mayotte during TAAF's Eparses Island rotation in April 2019.

Finally, one can also mention ESA's pre-operational program CYclone Monitoring Service based on Sentinel-1 (CYMS[10]), which is aiming at extending SAR acquisition to all TC basins and providing ocean surface winds over TC in real-time to demonstrate SAR potential for operational forecasting and to foster new scientific applications. This new program, motivated in large part by the results obtained in RNR-CYC, will allow to further understand the impact of TCs on Earth System cycles through answering fundamental questions on physical processes at play within these systems.

[10] https://www.esa-cyms.org

Author Contributions: Conceptualization OB and GB; software, CB, SB, PT, JP, JC and FC; data acquisition and processing, OB, GB, EC, ER, RC, GR, JD, AM, RH, SC, EL, DM and NM; writing—original draft preparation, OB, GB, EC, RC, ER, GR and CB; writing—review and editing, all co-authors; supervision, OB; project administration, OB; funding acquisition, OB, PT. All authors have read and agreed to the published version of the manuscript.

Funding: This research was principally funded by the European Union, the Regional Council of Reunion Island and the French State through INTERREG-V Océan Indien 2014-2020 projects "ReNovRisk-Cyclones and Climate Change" (TF) and "ReNovRisk Cyclones and Precipitation" (TF), as well as by Université de La Réunion and Centre National de la Recherche Scientifique (CNRS) in the frame of the "Contrat Plan Etat Région" (CPER) "ReNovRisk". The gliders were provided, operated and co-funded by CNRS DT-INSU (Direction Technique – Institut National des Sciences de l'Univers). The seismic stations deployed in the "Rivière des Pluies" network (code ZF) were provided by INSU-RESIF/SISMOB instrumental pool. The provision and operating of the BOREAL UAS were co-funded by Météo-France. The installation of GNSS stations on Eparses islands was funded by the Eparses consortium of the Terres Australes et Antarctiques Françaises (TAAF) administration under the frame of project "IOGA4MET-EI". Part of STORM operations were also co-funded by CNRS-INSU under the frame of the LEFE project "PreSTORM". Access to RADARSAT-2 data was supported by Institut Mines Télécom and by public funds (Ministère de l'Education Nationale, de l'Enseignement Supérieur et de la Recherche, FEDER, Région Bretagne, Conseil Général du Finistère, Brest Métropole) received in the framework of the VIGISAT project managed by Groupement Bretagne Télédétection (GIS BreTel – Brittany Remote Sensing).

Data Availability Statement: Part of the data used in this study are available in public repositories: https://scihub.copernicus.eu/ and https://cyclobs.ifremer.fr/ (S1 and RS2 SAR data); http://www.meteo.fr/temps/domtom/La_Reunion/webcmrs9.0/anglais/index.htm (best-track data); ftp://rgpdata.ign.fr/pub/gnssmayotte (GNSS data); http://seismology.resif.fr/ (seismic data - FDSN network codes PF and ZF). Other data used in this study are not publicly available yet due to temporary use restriction by data owners (these data, available on request from the corresponding author, will be soon deposited in the project's data repository).

Acknowledgments: The authors are grateful to the numerous students, researchers and engineers who participated in the field phase of the project, as well as to the staffs of IGN, for processing GNSS data, Kelonia, for equipping sea turtles, CNRS (DT-INSU), for operating the gliders, and Centre National de Recherches Météorologiques (CNRM, Météo-France) for operating the BOREAL UAS. The BOREAL UAS had been developed in the MIRIAD project (Système de Mesures scIentifiques de flux de suRface en mIlieu mAritime embarqué sur Drone), financed by the European Union and the Occitanie Region. The SHOC initiative has been possible thanks to SAR data access supported by ESA Sentinel-1 mission ground segment team and GIS BreTel. Sentinel-1 is part of the European space component of Copernicus European program. RADARSAT-2 is a commercial mission and data are provided by MDA's Geospatial Services (https://mdacorporation.com/geospatial/international). We are grateful to the OVPF (Observatoire Volcanologique du Piton de la Fournaise) and to IPGP colleagues who maintain the PF seismic stations and to F.R. Fontaine, E. Delcher and A. Gonzalez for the Riviere des Pluies seismic data acquisition (http://dx.doi.org/10.15778/RESIF.ZF2015). We would also like to warmly thank Mrs Sandrine Prunier and Nina Breznik, who successfully ensured the administrative management of this project.

Conflicts of Interest: The authors declare no conflict of interest.

References

1. Jiang, H., R. Oyama, O. Bousquet, J. L. Vigh and co-authors (2021). A Review of Tropical Cyclone Intensity Change (2014-2018). Part II: Rapid Intensification via Internal Influences. Submitted to *Atmosphere*.
2. Vigh, J. L., Y.-H. Huang, Y. Miyamoto, Q. Li et al. (2021). A Review of Intensity Change (2014-2018). Part III: Internal Influences". Submitted to *J. Meteorol. Soc. Japan*.
3. Courtney, J. B., S. Langlade, S. Barlow et al. (2019). Operational Perspectives on Tropical Cyclone Intensity Change Part 2: Forecasts by Operational Agencies. *Trop. Cyclone Res. Rev*, **8**, 226-239.
4. Heming, J., F. Prates, M. A. Bender et al. (2019). Review of recent progress in tropical cyclone track forecasting and expression of uncertainties. *Trop. Cyclone Res. Rev.*, **8**, 181-218.
5. Yablonsky R.M. (2016). Ocean Component of the HWRF Coupled Model and Model Evaluation. In: Mohanty U.C., Gopalakrishnan S.G. (eds) *Advanced Numerical Modeling and Data Assimilation Techniques for Tropical Cyclone Prediction*. Springer, Dordrecht. https://doi.org/10.5822/978-94-024-0896-6_10
6. Mogensen, K. S., L. Magnusson and J.-R. Bidlot (2017). Sensitivity of tropical cyclones to ocean coupling in the ECMWF coupled model. *J. Geophys. Res. Oceans* **122**, 4392–4412. doi: 10.1002/2017JC012753.
7. Feng, X, N. P. Klingaman and K. I. Hodges (2019). The effect of atmosphere–ocean coupling on the prediction of 2016 western North Pacific tropical cyclones. *Q. J. R. Meteorol. Soc.*, **145**: 2425– 2444. https://doi.org/10.1002/qj.3571
8. Vellinga, M., D. Copsey, T. Graham et al. (2020). Evaluating Benefits of Two-Way Ocean–Atmosphere Coupling for Global NWP Forecasts. *Wea. Forecast*., **35**, 2127–2144. doi: https://doi.org/10.1175/WAF-D-20-0035.1
9. Bousquet, O., M. Dalleau, M. Bocquet, P. Gaspar et al. (2020). Sea Turtles for Ocean Research and Monitoring: Overview and Initial Results of the STORM Project in the Southwest Indian Ocean. *Front. Mar. Sci.* **7**:594080. doi: 10.3389/fmars.2020.594080.
10. Leroux, M.-D., K. Wood, R. L. Elsberry et al. (2019). Recent Advances in Research and Forecasting of Tropical Cyclone Track, Intensity, and Structure at Landfall, *Trop. Cyclone Res. Rev.*, 7, 85-105. https://doi.org/10.6057/2018T CRR02.02.
11. Pianezze, J., C. Barthe, S. Bielli, P. Tulet et al. (2018). A new coupled ocean-waves-atmosphere model designed for tropical storm studies: example of Tropical Cyclone Bejisa (2013-2014) in the south-west Indian ocean. *J. Adv. Model. Earth Sys.*, **10**, doi:10.1002/2017MS001177
12. Pant, V. and K. R. Prakash (2020). Response of Air–Sea Fluxes and Oceanic Features to the Coupling of Ocean–Atmosphere–Wave During the Passage of a Tropical Cyclone. *Pure Appl. Geophys.* **177**, 3999–4023. https://doi.org/ 10.1007/s00024-020-02441-z
13. Prakash, K. R., V. Pant and T. Nigam (2019). Effects of the sea surface roughness and sea spray-induced flux parameterization on the simulations of a tropical cyclone. *J. of Geophys. Res. Atmospheres*, **124**: 14037– 14058. https://doi.org/10. 1029/2018JD029760
14. Mavume, A. F., L. Rydberg and J. R. E. Lutjeharms (2008). Climatology of tropical cyclones in the South-West Indian Ocean; landfall in Mozambique and Madagascar. *West. Indian Ocean J. Mar. Sci.* **8**: 15– 36.
15. Matyas, C. J. (2015). Formation and movement of tropical cyclones in the Mozambique channel. *Int. J. Climatol.* 35, 375–390. doi: 10.1002/joc.3985.
16. Leroux, M.-D., J. Meister, D. Mekies, A.L. Dorla, et al. (2018). A climatology of southwest Indian ocean tropical systems: their number, tracks, impacts, sizes, empirical maximum potential intensity, and intensity changes. *J. Appl. Meteorol. Climatol.*, **57**, 1021-1041.
17. Vialard, J., G. Foltz, M. McPhaden, J.-P. Duvel et al. (2008). Strong Indian Ocean sea surface temperature signals associated with the Madden-Julian Oscillation in late 2007 and early 2008. *Geophys. Res. Lett.* **35**:L19608. doi: 10.1029/2008GL035238
18. Hermes, J. C. and C. J. C. Reason (2009). The sensitivity of the Seychelles-Chagos thermocline ridge to large-scale wind anomalies. *ICES J. Mar. Sci.* **66**, 1455–1466. doi: 10.1093/icesjms/fsp074

19. Yokoi, T., T. Tozuka and T. Yamagata (2008). Seasonal variation in the Seychelles dome. *J. Clim.* **21**, 3740. doi: 10.1175/2008JCLI1957.1
20. Mawren, D., J. Hermes and C. J. C. Reason (2020). Exceptional Tropical Cyclone Kenneth in the Far Northern Mozambique Channel and Ocean Eddy Influences. *Geophys. Res. Lett.*, **47**, e2020GL088715. https://doi.org/10.1029/ 2020GL088715.
21. Emerton, R., H. Cloke, A. Ficchi, L. Hawker et al. (2020). Emergency flood bulletins for Cyclones IDAÏ and Kenneth: A critical evaluation of the use of global flood forecasts for international humanitarian preparedness and response, *Intern. J. Disast. Risk Reduc.*, **50**,101811, https://doi.org/10.1016/j.ijdrr. 2020.101811.
22. Matera, M. (2019). World Bank's Cyclone IDAÏ & Kenneth Emergency Recovery and Resilience Project 171040. http://documents1.worldbank.org/curated/en/72713156802 0768626/pdf/Project-Information-Document-Mozambique-Cyclone-IDAÏ-Kenneth-Emergency-Recovery-and-Resilience-Project-P171040.pdf
23. Tulet, P., B. Aunay, G. Barruol *et al.* (2021). ReNovRisk: a multidisciplinary programme to study the cyclonic risks in the South-West Indian Ocean. *Nat Hazards*, in press. https://doi.org/10.1007/s11069-021-04624-w
24. Sharmila, S. and K. J. E Walsh (2018). Recent poleward shift of tropical cyclone formation linked to Hadley cell expansion. *Nature Clim Change* **8,** 730–736. https://doi.org/10.1038/s41558-018-0227-5.
25. Camargo, S. J. and A. A. Wing (2021). Increased tropical cyclone risk to coasts. Science, **371**, 458-459. doi: 10.1126/science.abg3651.
26. Seidel, D., Q. Fu, W. Randel, W. et al. (2008). Widening of the tropical belt in a changing climate. *Nature Geosci* **1,** 21–24. https://doi.org/10.1038/ngeo.2007.38
27. Yang, H., G. Lohmann, J. Lu, E. J. Gowan et al. (2020). Tropical expansion driven by poleward advancing mid-latitude meridional temperature gradients. *J. Geophys. Res. Atmospheres*; 125, e2020JD033158. https://doi.org/10.1029/2020JD033158

28 Kossin, J. P., K. A. Emanuel and G. A. Vecchi (2014). The poleward migration of the location of tropical cyclone maximum intensity. *Nature* **509**:349–352. doi:10.1038/nature13278

29 Kossin, J. P., K. A. Emanuel and S. J. Camargo (2016). Past and projected changes in western North Pacific tropical cyclone exposure. *J Clim.*, **29**:5725–5739.

30 Sun, J., D. Wang, X. Hu, Z. Ling, et al. (2019). Ongoing poleward migration of tropical cyclone occurrence over the western North Pacific Ocean. *Geophys. Res. Lett.*, **46**, 9110– 9117. https://doi.org/10.1029/2019GL084260.

31 Krupar, R. J. and D. J. Smith (2019). Poleward Migration of Tropical Cyclone Activity in the Southern Hemisphere: Perspectives and Challenges for the Built Environment in Australia. In: *Collins J., Walsh K. (eds) Hurricane Risk. Hurricane Risk, vol 1*. Springer, Cham. https://doi.org/10.1007/978-3-030- 024 02-4_10

32. Cattiaux, J., F. Chauvin, O. Bousquet et al. (2020). Projected changes in the Southern Indian Ocean cyclone activity assessed from high-resolution experiments and CMIP5 models, *J. Climate*, **33**, 4975-4991. doi:10.1175/JCLI- D-19-0591.1
33. Barthe, C., O. Bousquet, S. Bielli et al. (2021). Impact of tropical cyclones on inhabited areas of the SWIO basin at present and future horizons: Modelling component of the research program RENOVRISK-CYCLONE. Submitted to *Atmosphere* (this special issue)
34. Bousquet, O., E. Lees, J. Durand et al. (2020). Densification of the Ground-Based GNSS Observation Network in the Southwest Indian Ocean: Current Status, Perspectives, and Examples of Applications in Meteorology and Geodesy, *Front. Earth Sci.* **8**:609757. doi: 10.3389/feart.2020.609757
35. Lees, E., O. Bousquet, D. Roy et al. (2020). Analysis of diurnal to seasonal variability of Integrated Water Vapour in the South Indian Ocean basin using ground-based GNSS and fifth-generation ECMWF reanalysis (ERA5) data. *Q. J. R. Meteorol. Soc.*, https://doi.org/10.1002/qj.3915.
36. Cesca, S., J. Letort, H. N. T. Razafindrakoto et al. (2020). Drainage of a deep magma reservoir near Mayotte inferred from seismicity and deformation. *Nat. Geosci.* **13**, 87–93. doi: 10.1038/s41561-019-0505-5

37. Davy, C., G. Barruol, F. R. Fontaine et al. (2014). Tracking major storms from microseismic and hydroacoustic observations on the seafloor. *Geophys. Res. Lett*., **41**, doi:10.1002/2014GL062319.
38. Davy, C., G. Barruol, G., F. R Fontaine and E. Cordier (2016). Analyses of extreme swell events on La Réunion Island from microseismic noise. *Geophys. J. Int*., **207**: 1767-1782, doi:10.1093/gji/ggw365.
39. Barruol, G., C. Davy, F. R. Fontaine et al. (2016). Monitoring austral and cyclonic swells in the "Iles Eparses" (Mozambique Channel) from microseismic noise. *Acta Oecologica*, **72**: 120-128, doi:10.1016/j.actao.2015.10.015.
40. Rindraharisaona, E. J., E. Cordier, G. Barruol, et al. (2020). Assessing swells in La Réunion Island from terrestrial seismic observations, oceanographic records and offshore wave models. *Geophys. J. Int*., **221**, 1883-1895, doi:10.1093/gji/ggaa117.
41. Rindraharisaona, E. J., G. Barruol, E. Cordier et al. (2021). Inferring cyclone signatures in the South-West of Indian Ocean from microseismic noise recorded on Réunion island. Submitted to *Atmosphere* (this special issue).
42. Bousquet, O, D. Barbary S. Bielli et al. (2020). An evaluation of tropical cyclone forecast in the Southwest Indian Ocean basin with AROME-Indian Ocean convection-permitting numerical weather predicting system. *Atmos Sci Lett*., 21:e950. https://doi.org/10.1002 /asl2.950.
43. Hsiao, L. F., D. S. Chen, J. S. Hong et al. (2020). Improvement of the Numerical Tropical Cyclone Prediction System at the Central Weather Bureau of Taiwan: TWRF (Typhoon WRF). *Atmosphere* **11**, 6: 657.
44. Takeuchi, Y. (2019): An Introduction of Advanced Technology for Tropical Cyclone Observation, Analysis and Forecast in JMA. *Trop. Cyclone Res. Rev.*, **7**, 153-163. https://doi.org/10.6057/2018TCRR03.01.
45. Mehra, A., V. Tallapragada, Z. Zhang et al. (2018). Advancing the State of the Art in Operational Tropical Cyclone Forecasting at NCEP. *Trop. Cyclone Res. Rev.*, **7**, 51-56. https://doi.org/10.6057/2018TCRR01.06
46. Davidson, N. E., Y. Xiao, Y. Ma et al. (2014). ACCESS-TC: Vortex specification, 4DVAR initialization, verification, and structure diagnostics. *Mon. Wea. Rev.*, **142**, 1265–1289. https://doi.org/10. 1175/MWR-D- 13-00062.1
47. Bender, M. A. and I. Ginis (2000). Real-case simulations of hurricane-ocean interaction using a high-resolution coupled model: Effects on hurricane intensity. *Mon. Wea. Rev.*, **128**, 917–946. https://doi.org/10.1175/1520-0493(2000)128<0917 :RCSOHO>2.0.CO;2
48. Black, W. J. and T. D. Dickey (2008). Observations and analyses of upper ocean responses to tropical storms and hurricanes in the vicinity of Bermuda, *J. Geophys. Res*., **113**, C08009, doi:10.1029/2007JC004358.
49. Price, J. F. (1981). Upper ocean response to a hurricane. *J. Phys. Ocean.*, **11**, 153–175. https://doi.org/10.1175/1520-0485(1981)011<0153:UORTAH>2.0.C O;2
50. Jullien, S., P. Marchesiello, C. E. Menkes et al. (2014). Ocean feedback to tropical cyclones: Climatology and processes. *Climate Dynamics*, **43**, 2831–2854. https://doi.org/10.1007/ s00382-014-2096-6
51. Smith, R. K., M. T. Montgomery and N. Van Sang (2009). Tropical cyclone spin-up revisited. *Q. J. R. Meteorol. Soc.*, **135**, 1321–1335. https://doi.org/10.1002/qj.428
52. Andreas, E. L. (2004). Spray stress revisited. *J. Phys. Ocean.*, **34**, 1429–1440. doi.org/10.1175/15200485(2004)034<1429:SSR>2.0.CO;2
53. Doyle, J. D. (2002). Coupled atmosphere-ocean wave simulations under high wind conditions. *Mon. Wea. Rev.*, **130**, 3087–3099. https://doi. org/10.1175/ 1520-0493 (2002) 130<3087:CAOWSU>2.0.CO;2
54. Andreas, E. L., J. B. Edson, E. C. Monahan et al. (1995). The spray contribution to net evaporation from the sea: A review of recent progress. *Boundary Layer Meteorol.*, **72**, 3–52. https://doi.org/10.1007/BF00712389
55. Wang, Y., J. D. Kepert and G. J. Holland (2001). The effect of sea spray evaporation on tropical cyclone boundary layer structure and intensity. *Mon. Wea. Rev.*, **129**, 2481–2500. https://doi.org/10.1175/1520-0493(2001)129<2481:TEOSSE>2.0.CO;2
56. Liu, B., H. Liu, L. Xie et al. (2011). A coupled atmosphere-wave-ocean modeling system: Simulation of the intensity of an idealized tropical cyclone. *Mon. Wea. Rev.*, **139**(1), 132–152. https://doi.org/ 10.1175/2010MWR3396.1

57. Richter, D. H. and D. P. Stern (2014). Evidence of spray-mediated air-sea enthalpy flux within tropical cyclones. *Geophys. Res. Lett.*, **41**, 2997–3003. https://doi.org/10.1002/2014GL059746
58. Andreas, E. L., L. Mahrt and D. Vickers (2015). An improved bulk air-sea surface flux algorithm, including spray-mediated transfer, *Q. J. R. Meteorol. Soc.*, **141**, 642-654
59. Ovadnevaite, J., A. Manders, G. de Leeuw, et al. (2014). A sea spray aerosol flux parameterization encapsulating wave state, *Atmos. Chem. Phys.*, **14**, 1837–1852, https://doi.org/10.5194/acp-14-1837-2014, 2014.
60. Willoughby, H., H.-L. Jin, S. J. Lord and J. M. Piotrowicz (1984). Hurricane structure and evolution as simulated by an axisymmetric, nonhydrostatic numerical model. *J. Atmos. Sci.*, **41**, 1169–1186.
61. Lord, S. J., H. E. Willoughby and J. M. Piotrowicz (1984). Role of a parameterized ice-phase microphysics in an axisymmetric, nonhydrostatic tropical cyclone model. *J. Atmos. Sci.*, **41**, 2836–2848. https://doi.org/10.1175/1520-0469(1984)041<2836:ROAPIP>2.0.CO;2
62. Wang, Y. (2002). An explicit simulation of tropical cyclones with a triply nested movable mesh primitive equation model: TCM3. Part II: Model refinements and sensitivity to cloud microphysics parameterization. *Mon. Wea. Rev.*, **130**(12), 3022–3036. https://doi.org/10.1175/1520-0493(2002)130<3022:AESOTC>2.0. CO;2
63. Zhu, T. and D. Zhang (2006). Numerical simulation of Hurricane Bonnie (1998). Part II: Sensitivity to varying cloud microphysical processes. *J. Atmos. Sci.*, **63**, 109–126. https://doi.org/10.1175/JAS3599.1
64. Li, J., G. Wang, W. Lin et al. (2013). Cloud-scale simulation study of Typhoon Hagupit (2008) Part II: Impact of cloud microphysical latent heat processes on typhoon intensity. *Atmospheric Research*, **120–121**, 202–215. https://doi.org/10. 1016/j.atmosres.2012.08.018
65. Hoarau T., C. Barthe, P.Tulet, M. Claeys (2018). Impact of the generation and activation of sea salt aerosols on the evolution of Tropical Cyclone Dumile. *J. Geophys. Res. Atmos.*, **123**, 8813-8831, doi:10.1029/2017JD028125.
66. Bielli S., C. Barthe, P. Tulet et al. (2021). The effect of atmosphere-ocean coupling on the structure and intensity of tropical cyclone Bejisa observed in the southwest Indian ocean. Submitted to *Atmosphere* (this special issue).
67. Thompson, C., C. Barthe, S. Bielli, P. Tulet, and J. Pianezze (2021). Projected Characteristic Changes of a Typical Tropical Cyclone under Climate Change in the South West Indian Ocean. *Atmosphere*, 12(2):232 - this special issue. https://doi.org/10.3390/atmos12020232.
68. Ferrario, F., M. W. Beck, C. D. Storlazzi et al. (2014). The effectiveness of coral reefs for coastal hazard risk reduction and adaptation. *Nature Communications*, **5**, 1– 9. https://doi.org/10.1038/ncomms4794
69. Lowe, R. J., J. L. Falter, M. D. Bandet et al. (2005), Spectral wave dissipation over a barrier reef, *J. Geophys. Res.*, **110**, C04001, doi:10.1029/2004JC002711.
70. van Dongeren, A., C. D. Storlazzi, E. Quataert and S. Pearson (2017). Wave dynamics and flooding on low-lying tropical reef-lined coasts. *Proceedings Coastal Dynamics 2017*, 654–664.
71. Pomeroy, A., R. Lowe, G. Symonds et al. (2012), The dynamics of infragravity wave transformation over a fringing reef, *J. Geophys. Res.*, **117**, C11022, doi :10.1029/2012JC008310.
72. Baldock, T. E, A. Golshani, D. P. Callaghan et al. (2014). Impact of sea-level rise and coral mortality on the wave dynamics and wave forces on barrier reefs. *Mar Pollut Bull.* **15**;83(1):155-64. doi: 10.1016/j.marpolbul.2014.03.058.
73. Pedersen, T. (2002). *Wave measurements using the PUV method* (Nortek (ed.); No. N4000-720; Issue 1). Nortek Group.
74. Hom-ma, M., K. Horikawa and S. Komori (1966). Response Characteristics of Underwater Wave Gauge. *Coastal Engineering in Japan*, **9**, 45–54. https://doi.org/10.1080/05785634.1966.11924671
75. Pomeroy, A. W. M., R. J. Lowe, M. Ghisalberti et al. (2018). Spatial variability of sediment transport processes over intratidal and subtidal timescales within a fringing coral reef system. *J. Geophys. Res. Earth Surface*, **123**, 1013–1034. https://doi.org/10.1002/2017JF004468

76. Smithers, S. G. and R. K. Hoeke (2014). Geomorphological impacts of high-latitude storm waves on low-latitude reef islands—observations of the December 2008 event on Nukutoa, Takuu, Papua New Guinea. *Geomorphology,* **222,** 106–21
77. Hoeke, R. K.; K. L. McInnes and J. G. O'Grady (2015). Wind and Wave Setup Contributions to Extreme Sea Levels at a Tropical High Island: A Stochastic Cyclone Simulation Study for Apia, Samoa. *J. Mar. Sci. Eng.,* **3**, 1117-1135. https://doi.org/10.3390/jmse3031117
78. Friedrich, A., F., K. Krüger and Klinge (1998). Ocean-generated microseismic noise located with the Gräfenberg array. *Journal of seismology*, **2**: 47-64.
79. Longuet-Higgins, M.S. (1950). A theory of the origin of the microseisms. *Phil. Trans. Roy. Soc.,* **243**: 1-35.
80. Ardhuin, F., L. Gualtieri and E. Stutzmann (2015). How ocean waves rock the Earth: Two mechanisms explain microseisms with periods 3 to 300 s. *Geophys. Res. Lett.*, **42**(3): 765-772, doi:10.1002/2014gl062782.
81. Barruol, G., D. Reymond, F. R. Fontaine et al. (2006). Characterizing swells in the southern Pacific from seismic and infrasonic noise analyses. *Geophys. J. Int*., **164**(3): 516-542, doi:10.1111/J.1365-246X.2006.02871.x.
82. Cessaro, R. K. (1994). Sources of primary and secondary microseisms. *Bull. Seismol. Soc. Amer*., **84**(1): 142-148.
83. Hasselmann, K. (1963). A statistical analysis of the generation of microseisms. *Rev. Geophys.*, **1**: 177-210.
84. Ardhuin, F., E. Stutzmann, M. Schimmel et al. (2011). Ocean wave sources of seismic noise. *J. Geophys. Res.*, **116**: C09004, doi:10.1029 /2011jc006952.
85. Essen, H.-H., F. Krüger, T. Dahm and I. Grevemeyer (2003). On the generation of secondary microseisms observed in northern and central Europe. *J. Geophys. Res.: Solid Earth*, **108**(B10): 2506, doi:10.1029/2002JB002338.
86. Obrebski, M.J., F. Ardhuin, E. Stutzmann and M. Schimmel (2012). How moderate sea states can generate loud seismic noise in the deep ocean. *Geophys. Res. Lett.*, **39**: L11601, doi:10.1029/2012gl051896.
87. Davy, C., E. Stutzman, G. Barruol, et al. (2015). Sources of secondary microseisms in the Indian Ocean. *Geophys. J. Int.*, **202**: 1180-1189, doi:10.1093/gji/ggv221.
88. Reading, A.M., K. D. Koper, M. Gal et al. (2014). Dominant seismic noise sources in the Southern Ocean and West Pacific, 2000–2012, recorded at the Warramunga Seismic Array, Australia. *Geophys. Res. Lett*., **41**(10), doi:10.1002/2014GL060073.
89. Beucler, E., A. Mocquet, M. Schimmel et al. (2014). Observation of deep water microseisms in the North Atlantic Ocean using tide modulations. *Geophys. Res. Lett.*: 2014GL062347, doi:10.1002/2014GL062347.
90. Bromirski, P. D. and F. K. Duennebier (2002). The near-coastal microseism spectrum: spatial and temporal wave climate relationships. *J. Geophys. Res.*, **107**(B8), doi:10.1029/2001JB000265.
91. Bromirski, P. D., F. K. Duennebier and R. A. Stephen (2005). Mid-ocean microseisms. *Geochem. Geophys. Geosyst.*, **6**: Q04009, doi:10.1029/2004 GC000768.
92. Chevrot, S., M. Sylvander, S. Benahmed et al. (2007). Source locations of secondary microseisms in western Europe: Evidence for both coastal and pelagic sources. *J. Geophys. Res.*, **112**(B11301), doi:10.1029/2007JB005059.
93. Koper, K.D. and R. Buriaciu (2015). The fine structure of double-frequency microseisms recorded by seismometers in North America. *J. Geophys. Res.*, **120**: 1677-1691, doi:10.1002/ 2014JB011820.
94. Tolman, H. L. and D. V. Chalikov (1996). Source terms in a third-generation wind wave model. *J. Phys. Oceanogr.*, **26**, 2497-2518.
95. Tolman, H. L. (2002). Distributed-memory concepts in the wave model WAVEWATCH III. *Parallel Computing*, **28**, 35-52, https://doi.org/10.1016 /S0167-8191(01)00130-2.
96. Perez, J., M. Menendez and I. J. Losada (2017) GOW2: A global wave hindcast for coastal applications. *Coastal Engineering*, **124**, 1–11.
97. Hasselmann, K., T. Barnett, E. Bouws et al. (1973). Measurements of wind-wave growth and swell decay during the Joint North Sea Wave Project (JONSWAP). *Deutsches Hydrographisches Institut.*

98. Harris, L., R. Nel, H. Oosthuizen et al. (2017). Managing conflicts between economic activities and threatened migratory marine species toward creating a multiobjective blue economy. *Conservation Biology*, **32**, 411-423. doi:10.1111/cobi.12992.
99. Swart, N. C., J. R. E. Lutjeharms, H. Ridderinkhof, and W. P. M. de Ruijter (2010), Observed characteristics of Mozambique Channel eddies, *J. Geophys. Res*., **115**, https://doi:10.1029/2009JC005875
100. Lutjeharms (2006). The Agulhas current. Springer. https://doi.org/ 10.1007/3-540-37212 -1
101. Lellouche, J.-M., E. Greiner, O. Le Galloudec and G. Garric, G. (2018). Recent updates of the Copernicus marine service's real-time global ocean monitoring and forecasting system 1/12° at high resolution. *Ocean Sci.* **14**, 1093–1126. doi: 10.5194/os-14-1093-2018
102. Cuypers, Y., X. Le Vaillant, P. Bouruet-Aubertot et al. (2013), Tropical storm-induced near-inertial internal waves during the Cirene experiment: Energy fluxes and impact on vertical mixing, *J. Geophys. Res. Oceans*, **118**, 358–380, doi:10.1029/2012JC007881.
103. Vialard, J., J-P. Duvel, M. McPhaden, P. Bouruet-Aubertot and co-authors (2009). Cirene: Air Sea Interactions in the Seychelles-Chagos thermocline ridge region, *Bull. Am. Met. Soc.*, **90**, 45-61.
104. Jaimes, B. and L.K. Shay (2009). Mixed layer cooling in mesoscale oceanic eddies during Hurricanes Katrina and Rita. *Mon. Wea. Rev.*, ***137***(12), 4188-4207. https://doi.org/10.1175/2009MWR2849.1
105. de Boyer Montégut, C., G. Madec, A.S. Fischer, et al. (2004), Mixed layer depth over the global ocean: An examination of profile data and a profile-based climatology, *J. Geophys. Res.*, **109**, 1-20, C12003, doi:10.1029/2004JC002378.
106. Holte, J. and L. Talley (2009). A new algorithm for finding mixed layer depths with applications to Argo data and subantarctic mode water formation. *Journal of Atmospheric and Oceanic Technology*, **26**, 1920–1939. https://doi.org/10.1175/2009JTECHO543.1
107. Tomczak, M. and J. S. Godfrey (2001) Regional oceanography—an introduction. *Butler & Tanner, London*
108. Pickard, G. L. and W. J. Emery (1990). Descriptive physical oceanography, *5th edn. Butterworth-Heinemann, Oxford*
109. Roberts, G., F. Burnet, S. Barrau, P. Medina et al. (2017). A drone over the oceans: the Miriad project. *La Météorologie*, **98**, 9-10, doi:10.4267/2042/62453, in French
110. Bevis, M., S. Businger, T. A. Herring, et al. (1992). GPS meteorology: Remote sensing of atmospheric water vapor using the global positioning system, *J. Geophys. Res.*, **97**, 15787–15801, doi:10.1029/92JD 01517.
111. Beutler, G. M. S. Rothacher, T. A. Schaer et al. (1999). The International GPS Service (IGS): An interdisciplinary service in support of earth sciences. *Adv. Space Res.*, **23**, 1999,1-635, doi:10.1016/S0273-1177(99)00160-X
112. Guerova, G., Jones, J., Douša, J., Dick et al. (2016). Review of the state of the art and future prospects of the ground-based GNSS meteorology in Europe, *Atmos. Meas. Tech*., **9**, 5385–5406, https://doi.org/10.5194/amt-9-5385-2016, 2016.
113. Dvorak, V. F. (1975). Tropical cyclone intensity analysis and forecasting from satellite imagery. *Mon. Wea. Rev.*, **103**, 420–430, https://doi.org/10.1175/1520 -0493(1975)103 <0420:TCIAAF>2.0.CO;2.
114. Brennan, M. J., C. C. Hennon, and R. D. Knabb (2009). The operational use of QuikSCAT ocean surface vector winds at the National Hurricane Center. *Wea. Forecasting*, **24**, 621–645, doi:10.1175/2008WAF2222188.1.
115. Chou, K.-H., C.-C. Wu, and S.-Z. Lin (2013): Assessment of the ASCAT wind error characteristics by global dropwindsonde observations. *J. Geophys. Res. Atmos.*, **118**, 9011–9021, doi:10.1002/jgrd.50724.
116. Mai, M., B. Zhang, X. F. Li, P. A. Hwang, and J. A. Zhang (2016). Application of AMSR-E and AMSR2 low-frequency channel brightness temperature data for hurricane wind retrievals. *IEEE Trans. Geosci. Remote Sens.*, **54**, 4501–4512, doi:10.1109/ TGRS.2016.2543502.
117. Zhang, L., X.-B. Yin, H.-Q. Shi, and Z.-Z. Wang (2016). Hurricane wind speed estimation using WindSat 6 and 10 GHz brightness temperatures. *Remote Sens.*, **8**, 721, doi:10.3390/rs8090721.
118. Reul, N., B. Chapron, E. Zabolotskikh, C. Donlon et al. (2017). A new generation of tropical cyclone size measurements from space. *Bull. Am. Meteor. Soc.*, **98** (11), 2367-2385, 10.1175/BAMS-D-15-00291.1

119. Monserrat, O, Crosetto M, Luzi G (2014). A review of ground-based SAR interferometry for deformation measurement. *ISPRS J. Photogramm Remote Sens.*, **93**, 40–48. https://doi.org/10.1016/j.isprsjprs.2014.04.001.

120 Fu, L. and B. Holt (1982). SEASAT views oceans and sea ice with Synthetic Aperture Radar. JPL Publ.. 81–120.

121. Li, X., J. A. Zhang, X. Yang, W. G. Pichel et al. (2013). Tropical cyclone morphology from spaceborne synthetic aperture radar, *Bull. Amer. Meteor. Soc.*, **94**, 215-230.

122. Young, G.; T. Sikora and N. Winstead (2008). Mesoscale Near-Surface Wind Speed Variability Mapping with Synthetic Aperture Radar. *Sensors*, **8**, 7012-7034. https://doi.org/10.3390/s8117012

123. Zhang, B. and W. Perrie (2012). Cross-Polarized Synthetic Aperture Radar: A New Potential Measurement Technique for Hurricanes, Bulletin of the American Meteorological Society, 93(4), 531-541

124. Mouche, A., B. Chapron, B., J. Knaff et al. (2019). Copolarized and cross-polarized SAR measurements for high-resolution description of major hurricane wind structures: Application to Irma category 5 hurricane. *J. Geophys. Research Oceans*, **124**, 3905–3922. https://doi.org/10.1029/2019JC015056.

125. Mouche, A., B. Chapron, B. Zhang and R. Husson (2017). Combined co- and cross-polarized SAR measurements under extreme wind conditions. *IEEE Xplore: IEEE Transactions on Geoscience and Remote Sensing*, **55**, 6476–6755.

126. Duong, Q.-P., S. Langlade, C. Payan et al. (2021). C-band SAR Winds for Tropical Cyclone monitoring and forecast in the South-West Indian Ocean. Submitted to *Atmosphere* (this special issue).

127. Sitkowski, M., J. P. Kossin and C. M. Rozoff (2011). Intensity and Structure Changes during Hurricane Eyewall Replacement Cycles. *Mon. Wea. Rev*. **139**, 3829–3847.

128. Willoughby, H., J. Clos and ML. Shoreibah (1982). "Concentric EyeWalls, Secondary Wind Maxima, and The Evolution of the Hurricane vortex". *J. Atmos. Sci*. **39**, doi:10.1175/1520-0469(1982)039<0395:CEWSWM>2.0.CO;2.

129. Madec, G., R. Bourdallé-Badie, and J. Chanuta (2019). *Nemo Ocean Engine. Notes From the Pôle de Modélisation.* France: Institut Pierre-Simon Laplace.

130. Barbary, D, M.-D. Leroux and O. Bousquet (2019). The orographic effect of Reunion Island on tropical cyclone track and intensity. *Atmos Sci Lett*.; 20:e882. https://doi.org/10.1002/asl.882